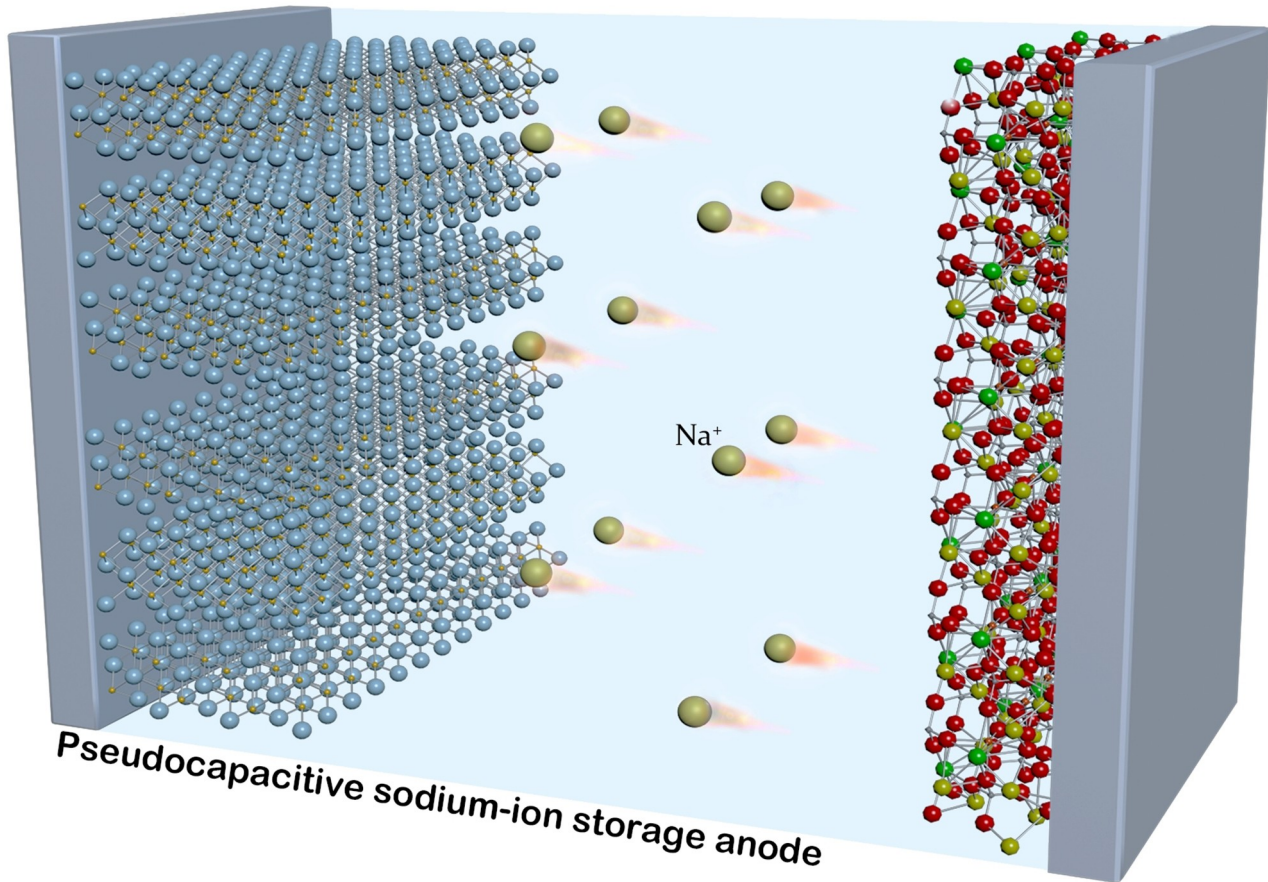


Special
Collection

Pseudocapacitive Anode Materials toward High-Power Sodium-Ion Capacitors

Xiaoqing Chang,^[a] Tingyi Huang,^[a] Jiayu Yu,^[a] Junbin Li,^[a] Jian Wang,^[a] and Qiu long Wei^{*[a]}

High-Power and High-Energy Sodium-Ion Capacitor



Sodium-ion storage technology holds great promise for large-scale, sustainable, and low-cost green energy storage systems. Overcoming the main limitations of sluggish Na^+ diffusion kinetics and achieving high-power sodium-ion storage devices is critical but full of challenges. Recently, emerging pseudocapacitive sodium-ion storage materials are attracting attention due to their superior rate capability and other comprehensive electrochemical performance. Herein, this review covers the charge storage mechanism, features, and performance of pseudocapacitive sodium-ion storage anode materials and the

assembled sodium-ion capacitors. The research processes of state-of-the-art pseudocapacitive sodium-ion storage anode materials, which display remarkable rate performance, high specific capacity and cycling stability, are introduced and discussed. Using the pseudocapacitive anode materials, advanced sodium-ion capacitors deliver high energy density at high power density. In the end, the outlooks of pseudocapacitive sodium-ion storage materials toward future high-power sodium-ion capacitors are briefly proposed.

1. Introduction

With the great demands for large energy supply and carbon emission reduction, the use of green energy (e.g. solar and wind energy) is rising rapidly.^[1] However, intermittent and unstable power delivery of green energy requires the cooperation with powerful energy storage systems to stabilize the continuous output day and night.^[2] Electrochemical energy storage (EES) devices are rapidly developed and applied in households and gigafactory. Battery and supercapacitor are two typical energy storage devices for world-wide applications.^[3,4] Lithium-ion batteries are widely applied in mobile electronics, electric vehicles and so forth, owing to their high energy density.^[5] But there are some limitations like low power density and unsatisfied cycle life.^[6] Supercapacitors can be ultra-rapidly charged in a few seconds, delivering high power density (over 10 kW kg^{-1}), and operate for tens of thousands of stable cycles, which are applied for hybrid electric vehicles, energy recovery in subway trains, and so forth.^[7,8] However, the energy density of traditional supercapacitors is limited. The developing direction of the next-generation EES devices is to realize both high energy and high power densities, ultralong cycle life, and low-cost.^[9]

In advanced EES devices, a combination of battery and supercapacitor is proposed to achieve both high energy and high power densities.^[10,11] The commercial supercapacitor (that is a symmetric electrical double-layer capacitor (EDLC)) suffers from insufficient energy density according to the nature of non-faradaic surface ion adsorption mechanism on both electrodes.^[12] Integrating faradaic reaction to build up non-aqueous symmetric capacitors is an effective strategy to obtain higher capacity and wider operation voltage, leading to a significant enhancement in energy density.^[13] A successful example is lithium-ion capacitors (LICs) through using lithium intercalation-type negative electrode (pre-lithiated graphite or

$\text{Li}_4\text{Ti}_5\text{O}_{12}$) and electrical double layer positive electrode (e.g. activated carbon (AC)), which deliver 4–5 times of energy density higher than that of EDLCs.^[14–16] The LICs are replacing the market of the traditional supercapacitors and lead-acid batteries in many fields, such as hybrid electric vehicles, public transports, automatic guided vehicles, energy recovery and gird storage systems.^[15]

Nevertheless, the resource of lithium is limited on earth and the cost is rapidly increasing, which could not satisfy all the requirements of large-scale uses.^[17,18] Alternatively, the sodium sources with abundance, geographic availability and long-term economic value make the sodium-ion storage technologies as promising candidates to substitute lithium-ion ones.^[19–21] Having the similar operation mechanism to LICs, traditional sodium-ion capacitors (SICs) are consist of the faradaic reacted anode and EDLC-type cathode.^[22] However, the radius of Na^+ is larger than Li^+ (1.02 vs. 0.76 Å), leading to the sluggish kinetics of Na^+ intercalation into anode material and the unmatched speed with rapid ion adsorption of EDLC-type cathode.^[23,24] It is necessary to develop faradaic-type anodes with rapid sodiation speed to balance the kinetics between the positive and negative sides.^[25]

Pseudocapacitive materials store charge through faradaic redox reaction on the surface or near-surface regions, offering a route for achieving both high specific capacity and high rate capability.^[22,26–28] Importantly, the pseudocapacitance exists not only in surface redox, but also in metal-ion intercalation (including Li^+ , Na^+ , K^+ , Zn^{2+} and so forth).^[29–32] The most studied example is the $\text{T-Nb}_2\text{O}_5$ with pseudocapacitive Li^+ intercalation behavior that is a solid-solution process without solid-state diffusion limitations.^[29,33] The pseudocapacitive lithium-ion storage anode materials show advantages for high-performance LICs. Recently, pseudocapacitive sodium-ion storage behaviors have been observed on various anode materials, such as TiO_2 ,^[34,35] $\text{FeVO}_4 \cdot n\text{H}_2\text{O}$,^[36] MXenes,^[37–39] MoS_2 ,^[40–42] TiN ,^[43] MoP ,^[44] and so forth, which showed remarkable high rate capability. In addition, the assembled SICs using pseudocapacitive anode materials displayed both high power and high energy performance.^[45,46]

Some valuable reviews focus on battery-type materials for metal-ion capacitors,^[47] pseudocapacitive storage mechanism and materials,^[9,22,26,27,48] and the hybrid ion capacitors.^[7,9] The pseudocapacitive sodium-ion storage anodes are emerging, and remain largely unexplored. It is timely to have a review

[a] X. Chang, T. Huang, J. Yu, J. Li, J. Wang, Prof. Q. Wei
 Department of Materials Science and Engineering
 Fujian Key Laboratory of Materials Genome

College of Materials
 Xiamen University
 Xiamen, 361005, Fujian, P. R. China
 E-mail: qlwei@xmu.edu.cn

An invited contribution to a Special Collection dedicated to Metal-Ion Hybrid Supercapacitors

that summarizes the novel pseudocapacitive sodium-ion storage anode materials and promotes the development of high-rate sodium-ion storage devices, especially for high-performance SICs. This review pays main attention to the pseudocapacitive anode materials, aiming to provide a clear and systematic understanding of the material structure, sodium-ion storage mechanism and electrochemical pseudocapacitive behavior of typical pseudocapacitive anode materials. Several typical pseudocapacitive materials are discussed in detail, including transition metal oxides, carbides (MXenes), sulfides, nitrides, phosphides, and vanadates. Then, the state-of-the-art assembled SICs based on the pseudocapacitive anode materials are briefly concluded. At the end of this review, we provide the summary and perspectives of pseudocapacitive anode materials and SICs in the future.

2. Electrochemical Mechanism and Features of Pseudocapacitive Sodium-Ion Storage Anode

It is of great importance to understand the detailed sodium-ion storage mechanism of active materials. The behaviors of battery-type anode material are classified into intercalation, conversion and alloying reactions.^[49–52] For the battery-type Na⁺ intercalation materials, the Na⁺ ions insert into the host materials and accompany with a phase transformation.^[53,54] The phase transformation exhibits obvious plateaus in the galvanostatic (dis)charge processes, according to sharp anodic and cathodic peaks in cyclic voltammetry (CV) measurement. There is a significant potential hysteresis (or called as overpotential) between the cathodic and anodic peaks in CV curves, and it increases with the acceleration of sweep rates.^[55–57] For conventional reaction materials, they suffer phase transformations from crystalline into amorphous, accompanied by nanosized transition metal clusters surrounded by sodium oxide matrixes at the totally sodiation state.^[58] During desodiation, these transition metal clusters are oxidized to form amorphous



Xiaoqing Chang is currently working toward his Ph.D. degree at the College of Materials, Xiamen University. He received his master degree from Nanjing University of Science and Technology in 2020. His research focuses on the sodium-ion batteries and sodium-ion capacitors.



Tingyi Huang received her bachelor degree from Fuzhou University in 2020. She is currently a master candidate at the College of Materials, Xiamen University. Her current research focuses on the sodium-ion storage materials and devices.



Jiayu Yu is currently a master candidate at the College of Materials, Xiamen University. He received his bachelor degree from Henan University of Science and Technology in 2020. His current research focuses on the nano-materials for sodium-ion storage.



Junbin Li is currently a master candidate at the College of Materials, Xiamen University, China. His research interests focus on electrochemical energy storage materials, particularly in layered oxides and poly-anion compounds.



Jian Wang is currently an undergraduate at the College of Materials, Xiamen University, China. His current research is the synthesis and optimization of energy storage materials for sodium-ion batteries.



Qilong Wei is currently an Associate Professor at Xiamen University. He received his Ph.D. from the State Key Laboratory of Advanced Technology for Materials Synthesis and Processing, Wuhan University of Technology in 2016 under the supervision of Prof. Qingjie Zhang and Prof. Liqiang Mai. He then joined the Department of Materials Science and Engineering at University of California, Los Angeles, as a Postdoctoral Researcher under the guidance of Prof. Bruce Dunn. His research focuses on design and synthesis of materials for electrochemical energy storage devices with both high energy and high power densities.

transition metal oxide. The CV curves show asymmetric redox behavior between the anodic and cathodic scans, and the significant potential hysteresis.^[58] The alloying reaction active materials involve multistep phase transformations, such as the Bi anode.^[59]

Differently, pseudocapacitive sodium-ion storage materials store charge based on a continuous change of their oxidation state without phase transformations.^[48] This process is a faradaic redox reaction in nature but shows fast kinetics. The pseudocapacitive sodium-ion storage behavior shows linear or pseudo-linear galvanostatic (dis)charge curves in a defined potential range. The CV curves of pseudocapacitive materials show box-like shape or very broad cathodic and anodic peaks with very small potential hysteresis (even at fast sweep rates). Different from the ideal linear relationship of C ($F\text{ g}^{-1}$) = dQ/dV for the EDLC, the C might be not a constant in the applied operating potential window for pseudocapacitive materials. Thus, it is encouraged to use the specific capacity (mAh g^{-1} or Cg^{-1}), areal capacity (mAh cm^{-2} or Ccm^{-2}) or volumetric capacity (mAh cm^{-3} or Ccm^{-3}) to evaluate the electrochemical performance of pseudocapacitive materials. The pseudocapacitive charge storage mechanism includes the underpotential deposition, surface redox pseudocapacitance and intercalation pseudocapacitance.^[26] Since the lacking report of underpotential deposition of sodium-ion storage, this review only includes the surface redox and intercalation pseudocapacitance. Surface redox pseudocapacitive sodium-ion storage indicates the faradaic redox happens on a limited region on/near surface (in several nanometers) of active materials,^[44,60] corresponding to a very short Na^+ diffusion distance and fast kinetics. Pseudocapacitive Na^+ intercalation involves rapid faradaic charge transfer with no crystallographic phase change, which is different from the battery-type intercalation with phase transformation.^[26]

The electrochemical behavior and reaction kinetics are related to their charge storage mechanisms, which could be analyzed based on CV measurements. The battery-type intercalation follows a semi-infinite diffusion-controlled process, in which the peak current (i_p) is proportional to the square root of sweep rate ($v^{1/2}$), according to the Randles-Sevcik equation [Eq. (1)].^[61]

$$i_p = 0.4463nFAcD^{1/2}v^{1/2} \left(\frac{\alpha nF}{RT} \right)^{1/2} \quad (1)$$

where n is the number of electrons, F is Faraday constant, A is surface area of the electrode material, c is surface concentration of the electrode material, D is the diffusion coefficient, v is sweep rate, α is transfer coefficient, R is molar gas constant and T is temperature.

Differently, the response current (i) of capacitive charge-storage materials is linear to the sweep rate, as described by Eq. (2).^[9]

$$i = vCA \quad (2)$$

A power law [Eq. (3)] is adopted to correlate the response currents (referred to as b -value analysis).^[9]

$$i(v) = av^b \quad (3)$$

where a is a constant and b is the power-law exponent. The $b=0.5$ indicates diffusion-controlled process and $b=1$ means capacitive charge storage process. Some materials showed the b values among 0.5 to 1, which might be owing to the concurrence of diffusion-controlled and capacitive reactions, or the influence of the limited electron transport caused by their poor electronic conductivities.^[46]

The total capacity (Q_{total}) of the active materials could be divided into surface-controlled and diffusion-controlled capacity [Eq. (4)].^[62]

$$Q_{\text{total}} = Q_{v=\infty} + \text{constant}(v^{-1/2}) \quad (4)$$

Capacity originated from surface controlled (capacitive) will be constant with the sweep rate, which means this part is independent even at high rates (named as $Q_{v=\infty}$). On the contrary, capacity followed semi-infinite diffusion-controlled process is linear to $v^{-1/2}$. Therefore, based on the CV measurements, the response current is the sum of surface capacitive and diffusion-controlled parts, as shown in Eq. (5).

$$i(v) = k_1v + k_2v^{1/2} \quad (5)$$

The k_1v is the surface capacitive contribution, and the $k_2v^{1/2}$ is diffusion-controlled part.^[63] The capacitive process is fast in nature and independent of the sweep rates, while the diffusion-controlled process is largely dependent on the tested sweep rates. In relative slow sweep rate ranges, using this method for evaluating the dominated charge storage process of active materials is closer to their intrinsic reaction mechanism.

Figure 1 shows the typical electrochemical performance of sodium-ion storage anode materials, including the battery-type $\text{Na}_2\text{Ti}_3\text{O}_7$ ^[64] and $\text{NaTi}_2(\text{PO}_4)_3$,^[65] and pseudocapacitive TiO_2 .^[66] The $\text{Na}_2\text{Ti}_3\text{O}_7$ anode displays distinct sodiated and desodiated plateaus at 0.2 and 0.4 V vs. Na^+/Na , respectively, accompanied by a reversible two-phase transformation (Figure 1a).^[64] The CV curves show very sharp cathodic/anodic peaks at 0.09/0.53 V vs. Na^+/Na at 0.2 mVs^{-1} (Figure 1b), corresponding to an overpotential of 440 mV. The overpotential is enlarged significantly with the increase of sweep rates. Using the b -value analysis, the b -value for the sodiation peak current is ~ 0.5 , corresponding to a diffusion-controlled process. Similar to $\text{Na}_2\text{Ti}_3\text{O}_7$, the NASICON material of $\text{NaTi}_2(\text{PO}_4)_3$ shows very flat cathodic/anodic plateaus at 2.11/2.14 V (Figure 1c), according to the reversible two-phase change between $\text{NaTi}_2(\text{PO}_4)_3$ and $\text{Na}_3\text{Ti}_2(\text{PO}_4)_3$.^[65] The CV curves show very separated cathodic and anodic peaks at 2.00 and 2.30 V at 0.2 mVs^{-1} , respectively, corresponding to an overpotential of 300 mV (Figure 1d). The b -value for the sodiation process is ~ 0.5 , which is a diffusion-controlled process.

Different from the battery-type materials, the pseudocapacitive sodium-ion storage of TiO_2 shows the pseudolinear (dis)charge curves (Figure 1e). The CV curves show a box-shape with a pair of broad cathodic and anodic peaks at 0.71 and

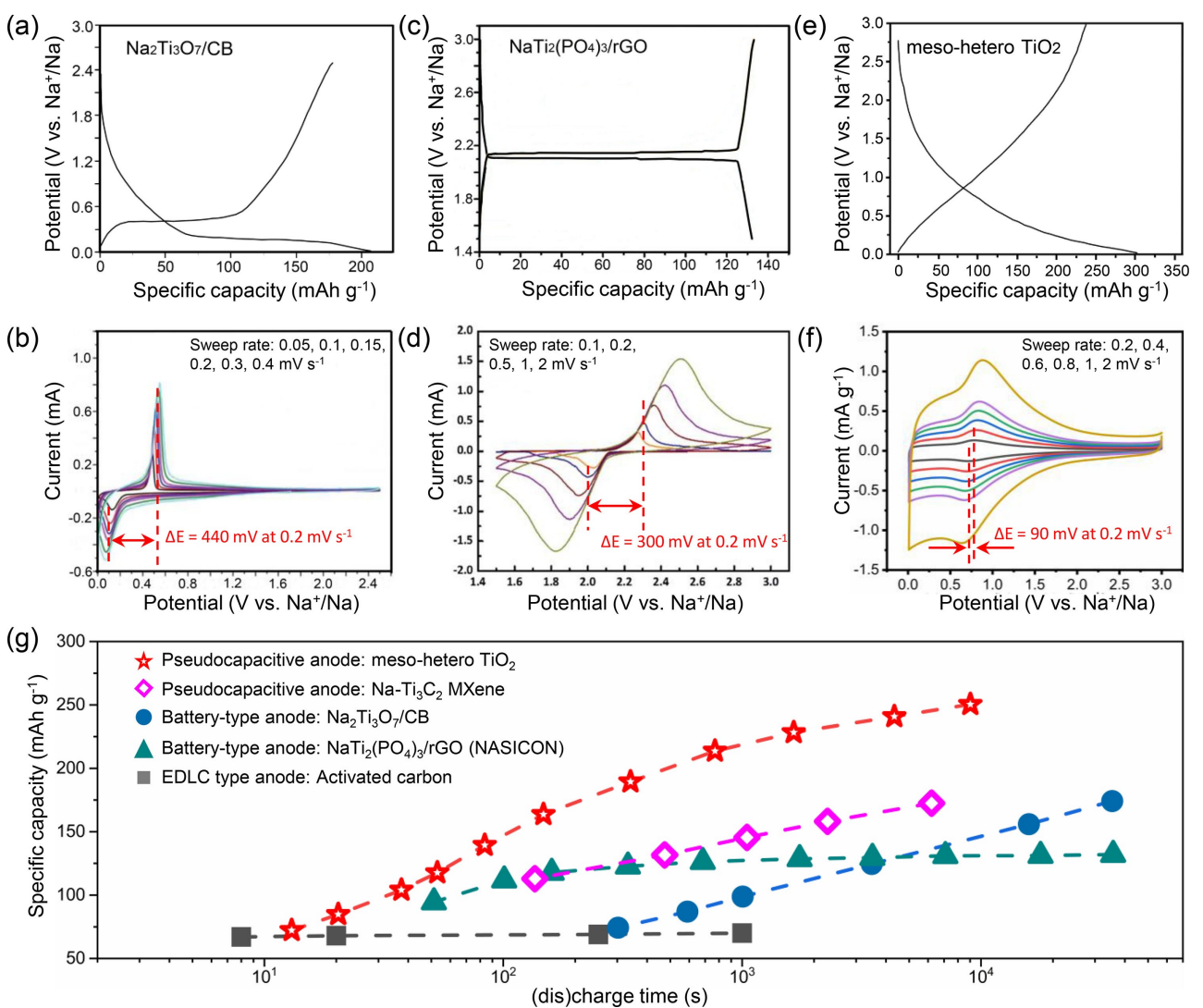


Figure 1. a) Galvanostatic (dis)charge curves and b) CV curves of battery-type $\text{Na}_2\text{Ti}_3\text{O}_7$ anode, respectively. Adapted from Ref. [64] with permission, Copyright (2013) Royal Society of Chemistry. c) Galvanostatic (dis)charge curves and d) CV curves of battery-type NASICON $\text{NaTi}_2(\text{PO}_4)_3$ anode, respectively. Adapted from Ref. [65] with permission, Copyright (2017) Royal Society of Chemistry. e) Galvanostatic (dis)charge curves and f) CV curves of pseudocapacitive meso-hetero- TiO_2 anode, respectively. Adapted from Ref. [66] with permission, Copyright (2019) American Chemical Society. g) Charge time vs. specific capacity profiles of reported anode materials: meso-hetero- TiO_2 , [66] $\text{Na}-\text{Ti}_3\text{C}_2$ MXene, [69] $\text{Na}_2\text{Ti}_3\text{O}_7/\text{CB}$, [64] and $\text{NaTi}_2(\text{PO}_4)_3/\text{rGO}$. [65] The pseudocapacitive TiO_2 and Ti_3C_2 -MXene anodes display excellent rate performance.

0.80 V at 0.2 mV s^{-1} , respectively, corresponding to a very small overpotential of 90 mV (Figure 1f). Similar broad peaks and slightly increased overpotential are observed with the increase of sweep rates. A huge overpotential of battery-type materials at a high rate will lead to a significant decrease in energy efficiency, while the pseudocapacitive materials with small overpotential are beneficial for delivering high energy density at high power.^[67,68] The (dis)charging time vs. specific capacity profiles (Figure 1g) show that the much higher specific capacity of pseudocapacitive TiO_2 ^[66] and $\text{Na}-\text{Ti}_3\text{C}_2$ MXene^[69] anodes in a shorter time.

3. Titanium Oxides

Titanium oxide (TiO_2) has been widely investigated as an anode material for lithium-ion batteries due to the high specific capacity, high safety and environmentally friendly. Among various phases, anatase TiO_2 (TiO_2 (A)) is considered as a lithium-ion insertion-type anode material, depended on a two-phase transition mechanism with a plateau of 1.75 V vs. Li^+/Li .^[70,71] Dunn and co-workers demonstrated that the contribution of pseudocapacitive lithium-ion storage in the ultrafine nanosized TiO_2 (A) nanoparticles (TiO_2 (A) NPs) (below 10 nm), which was regarded as an extrinsic pseudocapacitive material.^[26,34] Recently, many works have reported the applications of TiO_2 (A) for sodium-ion storage, interestingly, and some of the well-designed nano-materials/composites have exhibited pseudocapacitive behavior.

The understanding of sodium-ion storage mechanism is significantly important for optimizing the electrochemical performance. The detailed sodium-ion storage mechanism of TiO_2 (A) is needed to be discussed. Wu *et al.* investigated the sodium-ion storage behavior and mechanism of commercial TiO_2 (A) NPs (~ 30 nm, Sigma-Aldrich), while 1 M NaClO_4 in EC/PC (1:1 by volume) was used as the electrolyte.^[72] Based on *in-situ* X-ray diffraction (XRD) patterns (Figure 2a and b), the intensity of all the anatase diffraction peaks gradually decreased when it was sodiated to 0.3 V vs. Na^+/Na , corresponding to a decrease of crystallinity. Furthermore, all the diffraction peaks, except for the (101), disappeared at the end of totally sodiated at 0.1 V, indicating a partial transition of crystalline TiO_2 (A) into amorphous sodiated titania (Na_xTiO_2). In the subsequent desodiation step, the diffraction peaks of TiO_2 (A) were not recovered. Similarly, the amorphous transition of commercial TiO_2 (A) NPs (~ 25 nm, Sigma-Aldrich) in an ether-based electrolyte (1 M NaPF_6 in diglyme) was observed through *in-situ* XRD as well.^[73] As shown in Figure 2c, the (101) peak was almost not changed during sodiation from the open-circuit

potential (OCP) until to 0.5 V. During discharging from 0.25 to 0.01 V, the (101) peak disappeared gradually, which meant that the crystalline anatase phase lost its long-range ordering with the sodiation reaction. When charging back to 3.0 V, the anatase phase was not recovered, indicating an irreversible amorphization of crystalline TiO_2 (A). The sodium-ion storage of TiO_2 (A) might involve an irreversible amorphization process at the first sodiation step, and then the amorphous titanium oxide underwent reversible faradaic redox reactions with Na^+ ions.

When dealing with nanosized electrode materials, the influences of solid electrolyte interphase (SEI) layers need to be carefully considered.^[74] The SEI layers had a negligible influence on the lithium-ion storage of TiO_2 (A), whose operating potential (~ 1.75 V vs. Li^+/Li) was higher than the reduction/decomposition potential of most lithium-ion electrolytes.^[73] However, for sodium-ion storage, the operating potential of TiO_2 (A) anode was ~ 0 to 3.0 V vs. Na^+/Na . This potential window was usually accompanied by the severe decomposition of electrolytes and the formation of thick SEI layers, obviously, which has a great influence on the subsequent sodium-ion

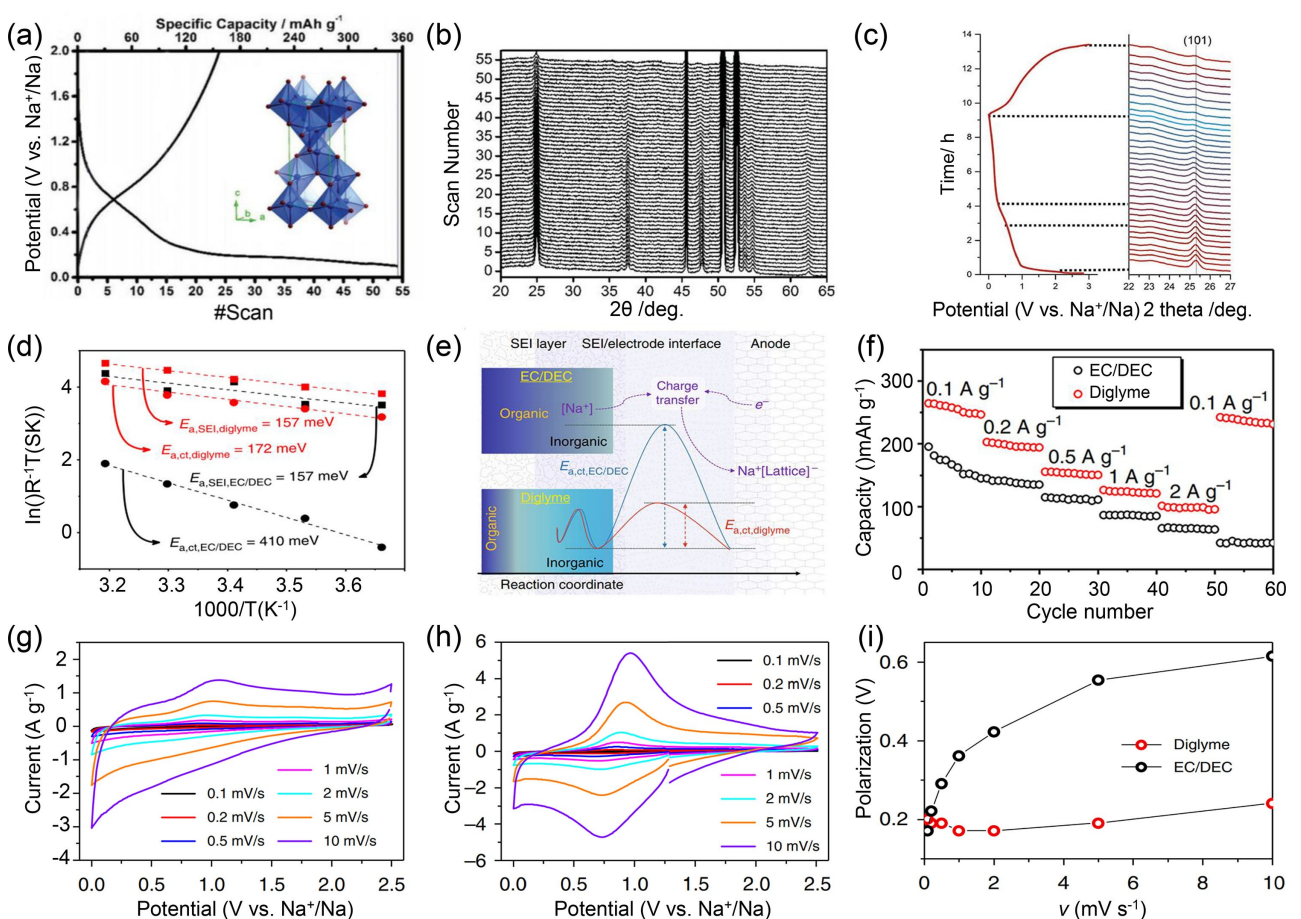


Figure 2. a) Galvanostatic (dis)charge curves and b) corresponding *in situ* XRD patterns of TiO_2 NPs (a size of ~ 30 nm) anode at 0.04 C (13.4 mA g^{-1}) in 0.1–2.0 V vs. Na^+/Na . Adapted from Ref. [72] with permission, Copyright (2015) Wiley-VCH. c) *In situ* synchrotron XRD patterns of the phase evolution for TiO_2 NPs (a size of ~ 25 nm) anode. Reprinted from Ref. [73] with permission, Copyright (2018) Wiley-VCH. d) Arrhenius plots of $E_{a,SEI}$ and $E_{a,ct}$ of TiO_2 NPs (a size of ~ 16 nm) in the diglyme and EC/DEC electrolytes. e) Schematic of the charge transfer energy barriers formed in diglyme and EC/DEC electrolytes. f) Rate performance of TiO_2 NPs in different electrolytes. CV curves of the TiO_2 anode measured in the electrolyte of g) 1 M NaCF_3SO_3 in EC/DEC and h) diglyme, respectively. i) The related potential polarization between the cathodic and anodic peaks from the CV curves (g and h) as a function of sweep rates. Reprinted from Ref. [75] with permission, Copyright (2019) The Authors.

storage performance. Relevant studies have proved that TiO_2 (A) electrodes exhibited enhanced performance in ether-based electrolyte rather than in carbonate-based electrolyte, owing to the less decomposition of electrolyte and formation of thinner SEI layers in the former one.^[73,75] Xu *et al.* investigated the electrochemical performance of the TiO_2 (A) in different electrolytes.^[73] They found the formation of thin (~2.5 nm) and stable SEI layers on titanium oxide in the ether-based electrolyte, but thick (~10 nm) and unstable SEI layers in the carbonate-based electrolyte. This difference was according to the higher lowest unoccupied molecular orbital energies of the Na^+/ether complexes. The more stable ether-based electrolyte led to much enhanced initial coulombic efficiency (ICE), cycling stability, significantly, and rate performance.

The activation energy (E_a) can be used to quantify the complex kinetics of sodium insertion into active materials.^[75] Based on the Arrhenius equation Li *et al.* collected the temperature-dependent impedance spectra and calculated the related activation energy of TiO_2 NPs (~16 nm, synthesized by solvothermal method) anode. As shown in Figure 2d, the $E_{a,\text{SEI,diglyme}}$ and $E_{a,\text{SEI,EC/DEC}}$ were both 157 meV, while the $E_{a,\text{ct,diglyme}}$ (ct means charge transfer) was much lower than $E_{a,\text{ct,EC/DEC}}$ (172 vs. 410 meV). Figure 2e schematically showed the SEI layers formed in ether-based (diglyme) and carbonate-based (EC/DEC) electrolyte, while the former exhibited a much lower charge transfer energy barrier, which meant Na^+ ions have faster kinetics in the ether-based electrolyte. Therefore, the TiO_2 electrode exhibited enhanced rate performance in the ether-based electrode than those in the carbonated-based electrolyte (Figure 2f). Impressively, Figure 2g and h showed the CV curves of TiO_2 electrodes at various sweep rates in the two different electrolytes, respectively. The fitting b -value of the redox peak currents was 0.85 in carbonate-based electrolyte, but it was 0.94 in the ether-based electrolyte. This meant that the diffusion-limited process through the SEI layers was inhibited and the pseudocapacitive response was enhanced when using ether-based electrolyte with thin SEI layers and low charge transfer energy barrier. Meanwhile, another benefit was the reduced polarization in the ether-based electrolyte (Figure 2i), which ensured high operation voltage at high rates (that was high power delivering).

The morphology of active materials has influence on electrochemical performance.^[76,77] Nanosheets-assembled heterostructural TiO_2 (A) spheres provided favorable Na^+ diffusion kinetics and exhibited pseudocapacitive performance.^[78] Recently, Lan and Wei *et al.* explored a bottom-up assembly strategy to synthesize two-dimensional (2D) mesoporous carbon@mesoporous TiO_2 @ mesoporous carbon sandwich-like heterostructure material (named as meso-hetero TiO_2).^[66] Continuous mesopores and highly uniform flake morphologies were observed by scanning electron microscopy (SEM) and transmission electron microscopy (TEM) images (Figure 3a). Figure 3b schematically shows the charge storage mechanism within this mesoporous heterostructure material. The interconnected large mesopores allowed the electrolyte to enter the interior adequately, which was very beneficial for the fast faradaic redox reaction between Na^+ and TiO_2 , and this two-

dimensional monolayer structure will greatly shorten the Na^+ diffusion path lengths. The galvanostatic (dis)charge profiles of the first cycle display an obvious slope-like curve (Figure 3c), which was typical pseudocapacitive behavior. The ICE was 79%, which was much higher than most sodium-ion storage anode materials.^[72–73,75]

The (dis)charge curves of the meso-hetero TiO_2 at specific currents from 1 to 50 A g^{-1} (Figure 3d) showed remarkable rate capability. The pseudocapacitive behavior accompanied with small potential polarization. Meanwhile, the CV curves at different sweep rates displayed broad redox peaks at ~0.8 V vs. Na^+/Na and small overpotentials (Figure 3e). Remarkably, according to the kinetics analysis and simulations, the meso-hetero TiO_2 exhibited 96.4% of total capacity from the capacitance contribution (Figure 3g), at a low sweep rate of 1 mVs^{-1} . The cycling performance of the meso-hetero TiO_2 was impressive, that was a capacity retention of 77.8% after 20,000 cycles at 10 A g^{-1} (Figure 3f). The galvanostatic (dis)charge curves presented a nearly triangular characteristic without potential decay at each cycle (inset of Figure 3f). The excellent electrochemical performance of the meso-hetero TiO_2 electrode is very promising for the construction of high-energy, high-power and long-cycle sodium-ion energy storage devices.

4. Vanadates

Vanadates, containing various types of open tunnel or layered structures, have been proved to exhibit promising lithium-ion and sodium-ion storage performance.^[79] The vanadates materials with highly tunable stoichiometric ratios, crystalline structures, element valances and micro/nano-morphologies could be designed as cathode or anode depended on their reaction potentials.^[80] Especially, the transition metal vanadates provide multi-electron charge transfer reactions based on the redox reaction of both vanadium and the transition metals (e.g., Zn,^[81] Co,^[82] Fe^[46,83] and so forth), leading to a high specific capacity.^[22,84]

Niederberger and co-workers reported the layered $\text{Zn}_{0.25}\text{V}_2\text{O}_5 \cdot n\text{H}_2\text{O}$ nanobelt/reduced graphene oxide composites (G-ZVO) delivered the initial sodiated and desodiated specific capacity of 609 and 364 mAh g^{-1} at 0.1 A g^{-1} in 0.01–3.0 V vs. Na^+/Na ,^[81] respectively. Interestingly, it was found the layered $\text{Zn}_{0.25}\text{V}_2\text{O}_5 \cdot n\text{H}_2\text{O}$ did not collapse even at the totally sodiated state (discharged to 0.01 V). They further synthesized the double-interlayer-cation metal vanadate $\text{Co}_{0.16}\text{Zn}_{0.09}\text{V}_2\text{O}_5 \cdot n\text{H}_2\text{O}$ nanobelts, which exhibited much enhanced electrochemical performance than the $\text{Zn}_{0.25}\text{V}_2\text{O}_5 \cdot n\text{H}_2\text{O}$ and $\text{Co}_{0.25}\text{V}_2\text{O}_5 \cdot n\text{H}_2\text{O}$ nanobelts.^[82] The kinetics analysis based on CV measurements revealed a large pseudocapacitive contribution of 83.9% to the total charge storage at 1 mVs^{-1} . The in-situ XRD patterns indicated the small lattice change of $\text{Co}_{0.16}\text{Zn}_{0.09}\text{V}_2\text{O}_5 \cdot n\text{H}_2\text{O}$ during cycling.

The ICE of the anode materials is very important for their practical use in full cells. Dong *et al.* reported the hydrated iron vanadate $\text{FeVO}_4 \cdot 0.6\text{H}_2\text{O}$ nanowires (NWs) with promising pseudocapacitive sodium-ion storage performance.^[83] Different

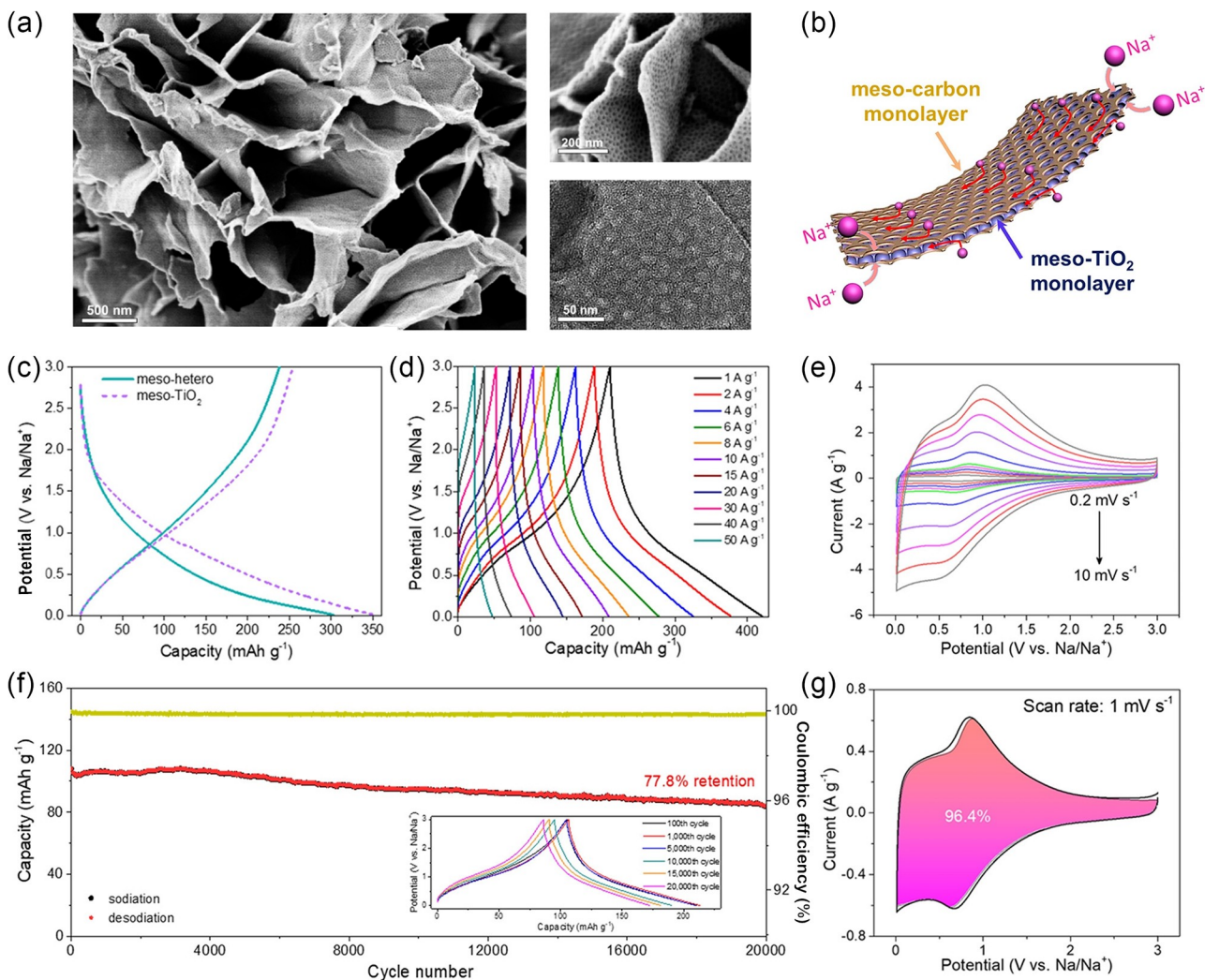


Figure 3. a) SEM and TEM images, and b) schematic of the sodium-ion storage process of meso-hetero TiO_2 , respectively. c) The initial (dis)charge curves of meso-hetero- TiO_2 and the meso- TiO_2 at 0.1 A g^{-1} . d) Galvanostatic (dis)charge curves of meso-hetero- TiO_2 at specific currents from 1 to 50 A g^{-1} . e) CV curves of meso-hetero- TiO_2 at various sweep rates from 0.2 to 10 mV s^{-1} . f) Cycling performance of meso-hetero- TiO_2 for 20,000 cycles at 10 A g^{-1} ; the inset is the corresponding (dis)charge curves at different cycles. g) Separation of the capacitive and diffusion currents for the meso-hetero- TiO_2 at 1 mV s^{-1} . Reprinted from Ref. [66] with permission, Copyright (2019) American Chemical Society.

from the $\text{Zn}_{0.25}\text{V}_2\text{O}_5 \cdot n\text{H}_2\text{O}$ nanobelts, the crystalline $\text{FeVO}_4 \cdot 0.6\text{H}_2\text{O}$ NWs anode turned into amorphous when cycled below 1 V vs. Na^+/Na . But, when cycled in the window of 1.0–3.0 V, $\text{FeVO}_4 \cdot 0.6\text{H}_2\text{O}$ underwent a solid-solution reaction during the (de)intercalation of Na^+ ions, as confirmed by in-situ XRD and ex-situ high-resolution TEM (HRTEM). The $\text{FeVO}_4 \cdot 0.6\text{H}_2\text{O}$ anode delivered a high ICE of 83%, a reversible sodiation capacity of 169 mAh g^{-1} at 0.1 A g^{-1} and 40 mAh g^{-1} at 10 A g^{-1} , and stable 2000 cycles. According to the quantitative kinetics analysis, 93% of total capacity was from capacitive contribution at the sweep rate of 1 mV s^{-1} . Further, ultrathin layered iron vanadate ($\text{Fe}_3\text{V}_{15}\text{O}_{39}(\text{OH})_9 \cdot 9\text{H}_2\text{O}$) nanosheets (named as FeVO UNSs) were synthesized by a facile sonicate-assisted method.^[46] The novel layered FeVO UNSs anode delivered rapid and reversible Na^+ (de)intercalation in the potential window of 0.8–3.4 V (Figure 4a). The (dis)charge curves (Figure 4b) were quasi-linear-like and well overlapped. The initial sodiation and desodiation capacity were 322 and 303 mAh g^{-1} , respectively.

The corresponding ICE was 93.86%, which was much higher than the reported state-of-the-art pseudocapacitive storage anodes (as summarized in Table 1). In-situ synchrotron high-energy XRD patterns (Figure 4c) and ex-situ SEM image (Figure 4d) indicated the very stable layered structure of FeVO UNSs during the sodiation process. The CV curves of FeVO UNSs (Figure 4e) showed box-like shapes with broad redox peaks, which was typical pseudocapacitance behavior. The redox peaks slightly shifted with the enlarged sweep rates, indicating fast reaction ability. The charge storage was pseudocapacitive-dominated Na^+ intercalation process (a capacitive contribution of 81.6% at 0.2 mV s^{-1} , Figure 4f), with no phase changes in 0.8–3.4 V. The (dis)charge curves at different specific currents (Figure 4g) were all linear-like, and a high specific capacity of 80 mAh g^{-1} was obtained at 20 A g^{-1} . The unique ultrathin nanosheet morphology provided a much better rate performance than that of FeVO nanosheets-assembled flowers. The FeVO UNSs showed the capacity

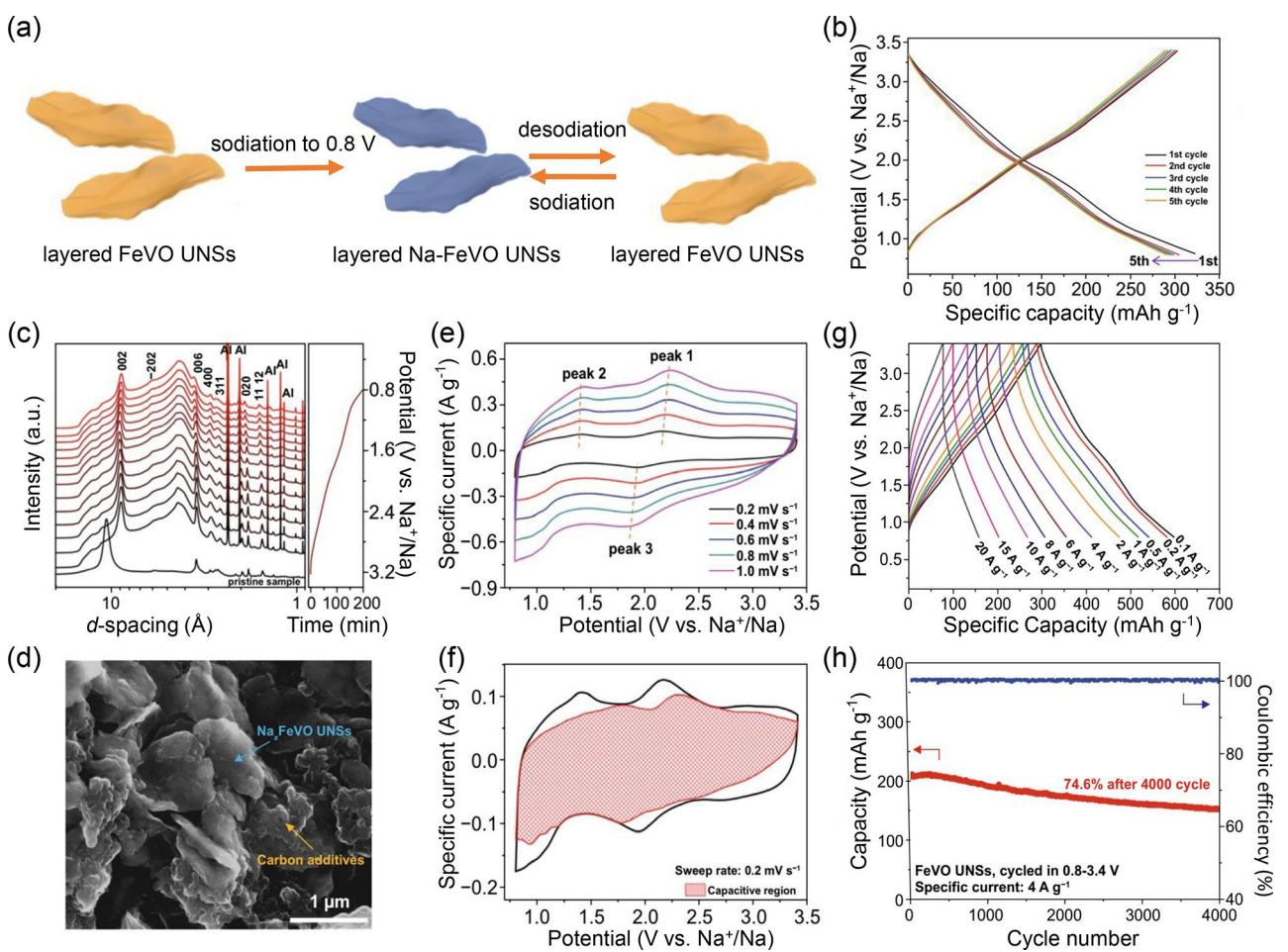


Figure 4. a) Schematic of sodium-ion storage mechanism for FeVO UNSs in 0.8–3.4 V. b) Galvanostatic (dis)charge curves cycled at 0.1 A g^{-1} in 0.8–3.4 V. c) *In situ* synchrotron XRD patterns during sodiation to 0.8 V. d) *Ex situ* SEM image after cycled in 0.8–3.4 V. e) CV curves of FeVO UNSs anode in 0.8–3.4 V at different sweep rates. f) Separation of capacitive contribution (shaded area) at 0.2 mV s^{-1} . g) (dis)charge curves of FeVO UNSs at different specific currents. h) Cycling performance of FeVO UNSs at 4 A g^{-1} . Reprinted from Ref. [46] with permission, Copyright (2021) The Authors.

retention of ~75% after 4000 cycles at a high specific current of 4 A g^{-1} (Figure 4h). The FeVO UNSs anode is ideal for developing next-generation economical electrochemical energy storage devices.

5. Transition Metal Sulfide

MoS_2 is one kind of layered material that consists of stacked S–Mo–S layers through Van der Waals force.^[85] According to the relative position of the S atomic layer, the MoS_2 has two phases: 2H (trigonal prismatic, D_{3h}) and 1T phase (octahedral, O_h).^[86] 2H– MoS_2 is a semi-conductor phase, in which the position of two S atom layers is completely staked in the top view.^[87] 1T– MoS_2 is the metallic phase, in which one S atom layer is located at the center of hexagon composed of Mo and another S atom layer. These two phases could interconvert through the sliding of the S atomic layer under heat treatment or alkali-metal ion intercalation.^[86]

Layered MoS_2 could be a host material for sodium-ion storage, and the detailed mechanism was systematically

investigated by *in-situ* XRD, the advanced aberration-corrected scanning transmission electron microscopy (STEM), and the *ex-situ* grazing incidence small angle scattering (GISAX).^[40,87,88] The initially total sodiation (sodiated until to the potential of $\sim 0 \text{ V}$ vs. Na^+/Na) of commercial 2H– MoS_2 particles (the SEM image as shown in Figure 5a) involved three steps (Figure 5b): (1) a phase transition from 2H– MoS_2 ($a=3.16 \text{ \AA}$ and $c=12.29 \text{ \AA}$) to 2H– $\text{Na}_{0.5}\text{MoS}_2$ ($a=3.21 \text{ \AA}$ and $c=15.06 \text{ \AA}$) with a plateau at $\sim 0.85 \text{ V}$; (2) a phase transition (Figure 5c) from 2H– $\text{Na}_{0.5}\text{MoS}_2$ to 1T– NaMoS_2 ($a=3.11 \text{ \AA}$ and $c=14.29 \text{ \AA}$) with a plateau at $\sim 0.75 \text{ V}$, and the additional intercalation of Na^+ into Na_xMoS_2 ($1.0 < x < 1.5$) with negligible structure changes upon the potential of 0.4 V ; (3) a conversion reaction that the layered Na_xMoS_2 lost its crystalline and totally turned into metallic Mo and Na_xS until the potential close to $\sim 0 \text{ V}$, which was irreversible. Controlling the operation potential window in 0.8–2.5 V, the phase transition between 2H– MoS_2 and 2H– $\text{Na}_{0.5}\text{MoS}_2$ was highly reversible, accompanied by the sodiation and desodiation plateaus for 100 cycles.^[88] When cycled in the potential range of 0.4–2.5 V, the phase transitions from 2H– MoS_2 to 2H– $\text{Na}_{0.5}\text{MoS}_2$ then to 1T– Na_xMoS_2 ($1 < x <$

Active materials	Electrode composition	Mass loading [mg/cm ²]	Electrolyte	Operating potential window [V vs. Na ⁺ /Na]	ICE [%]	Rate performance	Cycling performance (capacity retention)	Ref.
TiO ₂ (A) NPs = 7:1.5:1.5	AM:CB:PVD ^F	—	1 M NaCF ₃ SO ₃ DEGDME	0.005–2.5	69	252 mAhg ⁻¹ at 0.1 A g ⁻¹ (15.1 min) 153 mAhg ⁻¹ at 0.5 A g ⁻¹ (18.4 min) 99 mAhg ⁻¹ at 2 A g ⁻¹ (2.97 min)	68.22% ^[b] after 500 cycles at 0.1 A g ⁻¹	[75]
AM:CB:PVD ^F = 7:1.5:1.5	AM:CB:EC ₅₀ : DEC ₅₀	—	1 M NaCF ₃ SO ₃ EC ₅₀ :	0.005–2.5	33	165 mAhg ⁻¹ at 0.1 A g ⁻¹ (99 min) 113 mAhg ⁻¹ at 0.5 A g ⁻¹ (8.2 min) 66 mAhg ⁻¹ at 2 A g ⁻¹ (1.98 min)	48.52% ^[b] after 500 cycles at 0.1 A g ⁻¹	[75]
meso-hetero-TiO ₂ SBR	AM:CB:CMC: = 8:10:5:0.5	—	1 M NaPF ₆ DEGDME	0–3.0	79	160 mAhg ⁻¹ at 4 A g ⁻¹ (2.4 min) 160 mAhg ⁻¹ at 20 A g ⁻¹ (0.22 min) 73 mAhg ⁻¹ at 20 A g ⁻¹ (0.22 min)	77.8% after 20000 cycles at 10 A g ⁻¹	[66]
Ti ₃ C _x MXene	AM:KIB:PVD ^F = 8:1:1	—	1 M NaPF ₆ EC ₅₀ :DEC ₅₀	0.1–3.0	46	111 mAhg ⁻¹ at 0.02 A g ⁻¹ (333 min) 70 mAhg ⁻¹ at 0.5 A g ⁻¹ (8.4 min)	80.64% ^[b] after 100 cycles at 0.02 A g ⁻¹	[98]
Ti ₃ C _x MXene/ CNT-SA	—	—	1 M NaClO ₄ EC _{47.5} : PC _{47.5} :FEC ₅	0.01–3.0	35.7	425 mAhcm ⁻³ at 0.02 A g ⁻¹ 266 mAhcm ⁻³ at 0.5 A g ⁻¹	106.48% ^[b] after 500 cycles at 0.1 A g ⁻¹	[100]
Na-Ti ₃ C _x MXene = 7:1.5:1.5	AM:AB:PAA	—	1 M NaClO ₄ EC _{47.5} : PC _{47.5} :FEC ₅	0–3.0	63	189 mAhg ⁻¹ at 0.1 A g ⁻¹ (11.3 min) 113 mAhg ⁻¹ at 3 A g ⁻¹ (2.26 min)	92.39% ^[b] after 2000 cycles at 2 A g ⁻¹	[69]
US-Mo ₂ -NSs @NG	AM:CB: PVDF = 7:2:1	0.8–1.0	1 M NaClO ₄ EC ₄₅ : DEC ₄₅ :FEC ₁₀	0.4–3.0	71.15	271 mAhg ⁻¹ at 0.1 A g ⁻¹ (16.3 min) 175 mAhg ⁻¹ at 3.2 A g ⁻¹ (3.3 min)	86.84% after 1000 cycles at 1 A g ⁻¹	[42]
MoS ₂ microflower	AM:AB: PVDF = 8:1:1	0.73–0.91	1 M NaPF ₆ EC _{47.5} : DEC _{47.5} :FEC ₅	0.4–3.0	60.67	141 mAhg ⁻¹ at 12.8 A g ⁻¹ (0.66 min) 124 at 1 A g ⁻¹ (7.14 min)	86.7% after 800 cycles at 1 A g ⁻¹	[115]
MoP/C mesopo- rous NWs	AM:KIB: CMC = 7:2:1	1–1.5	1 M NaPF ₆ DEGDME	0.05–3.0	77.3	62 mAhg ⁻¹ at 10 A g ⁻¹ (0.372 min) 293 mAhg ⁻¹ at 0.1 A g ⁻¹ (17.6 min)	56.99% after 3500 cycles at 1 A g ⁻¹	[44]
Ti(O,N) mesopo- rous NWs	AM:CMC = 9:1	1–1.5	1 M NaClO ₄ EC _{47.5} : DMC _{47.5} :EC ₅	0.02–3.0	43	107 mAhg ⁻¹ at 0.05 A g ⁻¹ (128 min) 67 mAhg ⁻¹ at 0.1 A g ⁻¹ (40 min)	73% after 5000 cycles at 1 A g ⁻¹	[43]
Meso-Mo ₃ N ₂ -NWs	AM:AB: CMC = 8.5:10:5	1–1.5	1 M NaClO ₄ EC _{47.5} : DMC _{47.5} :FEC ₅	0.01–3.0	80.4	35 mAhg ⁻¹ at 8 A g ⁻¹ (0.26 min) 278.9 mAhg ⁻¹ at 0.1 A g ⁻¹ (16.7 min)	78.6% after 800 Cycles at 1 A g ⁻¹	[107]
FeVO ₄ ·0.6H ₂ O NWs	AM:CC: CMC = 8:1.2:0.8	~1	1 M NaPF ₆ DEGDME	1.0–3.0	83	168.75 mAhg ⁻¹ at 4 A g ⁻¹ (2.53 min) 87 mAhg ⁻¹ at 16 A g ⁻¹ (0.33 min)	83% after 2000 cycles at 0.04 A g ⁻¹	[83]
FeVO UNSS	AM:CC:CMC: SBR = 75:15:5:5	1.5–2.0	1 M NaPF ₆ DEGDME	0.8–3.4	93.86	127 mAhg ⁻¹ at 1 A g ⁻¹ (7.6 min) 40 mAhg ⁻¹ at 10 A g ⁻¹ (0.24 min) 175 mAhg ⁻¹ at 6 A g ⁻¹ (1.75 min) 80 mAhg ⁻¹ at 20 A g ⁻¹ (0.24 min)	74.6% after 4000 cycles at 4 A g ⁻¹	[46]

[a] ICE: initial coulombic efficiency; AM: active material; CB: carbon black; AB: acetylene black; PAA: polyacrylic acid; PVDF: polyvinylidene fluoride; CMC: carboxymethyl cellulose; NG: nitrogen-doped graphene; DEGDME: diethylene glycol dimethyl ether; EC: ethylene carbonate; DMC: dimethyl carbonate; FEC: diethyl carbonate; DEC: diethyle carbonate; PC: propylene carbonate. [b] The cycling performance were calculated based on the original data of cycling plots.

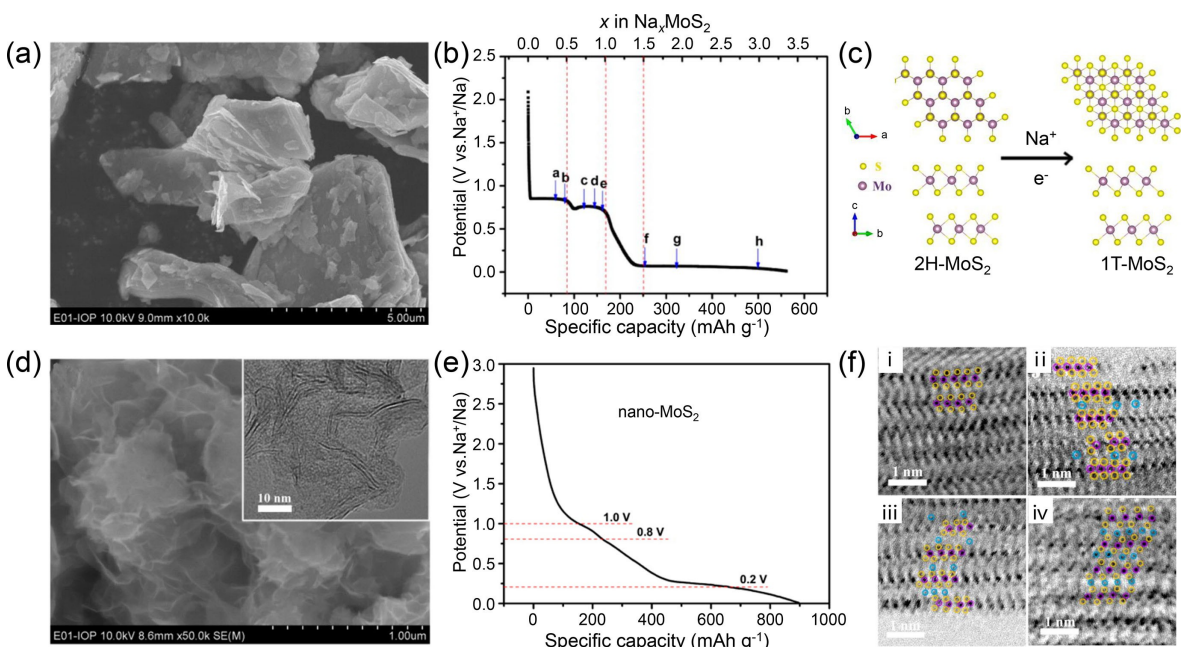


Figure 5. a) SEM image and b) initial sodiation curve of commercial MoS_2 , respectively. d) SEM image and e) initial sodiation curve of home-prepared nanoscaled MoS_2 , respectively. c) The schematic of phase transition from 2H to 1T MoS_2 after Na^+ intercalation. f) The annular brightfield (ABF) images of as-prepared nano- MoS_2 (i), with cutoff at 1.0 V (ii), 0.8 V (iii), and 0.2 V (iv) along the [100] zone axis. Reprinted from Ref. [87] with permission, Copyright (2013) American Chemical Society.

1.5) were irreversible.^[87] After the initial several cycles, the 2H- MoS_2 was converted into the metallic 1T- MoS_2 based on the intercalation of Na^+ . Then, the initial sodiation and desodiation plateaus were disappeared, and linear slope-like curves (pseudocapacitive behavior) were displayed which was based on a solid-solution reaction of the 1T- NaMoS_2 .^[40,88]

Nanosized MoS_2 (Figure 5d) exhibited much different initial sodiation behavior to the MoS_2 bulks, that was a pseudo-linear slope curve (without the above-mentioned reaction plateaus) in the first discharge step (Figure 5e).^[87] But, the nano- MoS_2 also involved the phase transition from 2H to 1T phase, as demonstrated by the annular bright-field (ABF) imaging technique (Figure 5f). It was found that the intercalated Na^+ firstly occupied every other interlayer and the other ones remained empty (Figure 5f(ii)). Then, the additionally intercalated Na^+ started to fill the empty interlayers, and the sulfur planes glided along an intralayer atomic plane to form 1T- MoS_2 (Figure 5f(iii)). The fulfills of Na^+ in the interlayer were observed (Figure 5f(iv)). The nanostructured MoS_2 displayed an effective route to overcome its sluggishly step-by-step battery-type phase transitions, achieving rapid pseudocapacitive sodium-ion storage.

Tolbert and co-workers reported the ordered mesoporous MoS_2 (mp- MoS_2) thin-film (Figure 6a) as the sodium-ion storage anode.^[40] The initial CV curve of the mp- MoS_2 (Figure 6b) showed a broad cathodic peak at 0.90 V, corresponding to the conversion into 1T- MoS_2 phase. The box-like CV shape and small overpotential with the increasing sweep rates indicated an excellent pseudocapacitive behavior of mp- MoS_2 (Figure 6c). According to Trasatti analysis method [Eqs. (6) and (7)],^[40]

$$q(v) = q_{\text{capacitive}} + \alpha(v^{-1/2}) \quad (6)$$

$$\frac{1}{q(v)} = \frac{1}{q_{\text{tot}}} + \alpha(v^{1/2}) \quad (7)$$

the capacitive capacity $q_{\text{capacitive}}$ was calculated to be 96 mAh g^{-1} (Figure 6d) and the total capacity $q_{\text{tot}} \approx 130 \text{ mAh g}^{-1}$ (Figure 6e). The capacitive charge storage contributed 74% of the total capacity. Besides, according to the quantitative kinetics analysis and simulations, 82% of total capacity was from the capacitance contribution (Figure 6f) at the sweep rate of 1 mV s^{-1} , which was in good agreement with the Trasatti analysis result.

Expanding the interlayer spacing of MoS_2 would promote the Na^+ diffusion kinetics and enhance the rate capability. Hu *et al.* synthesized the MoS_2 nanoflowers (FG- MoS_2 , Figure 6g) and well-crystallized MoS_2 (CG- MoS_2) for sodium-ion storage.^[41] The interlayer spacing of nanosized FG- MoS_2 (0.67 nm) and CG- MoS_2 (0.64 nm) was larger than that of the MoS_2 bulk (B- MoS_2 , 0.62 nm). The FG- MoS_2 and CG- MoS_2 displayed slope-like (dis)charge curves without any plateaus (Figure 6h). The FG- MoS_2 delivered remarkable rate performance (Figure 6i) and excellent cycling performance. Huang *et al.* synthesized methyl-functionalized MoS_2 (m- MoS_2) with the conversion into 1T phase after the second solvothermal treatment, which could inhibit the irreversible phase transition under the electrochemical reaction.^[89] The expanded interlayer spacing (0.8 nm) suppressed the lattice breathing of MoS_2 structure during Na^+ (de)intercalation, leading to enhanced structural and cycling stability. Zhang *et al.* explored the effect of interlayer spacing on the electrochemical performance of MoS_2 anode materials.^[90] They prepared tunable interlayer spacing ranging

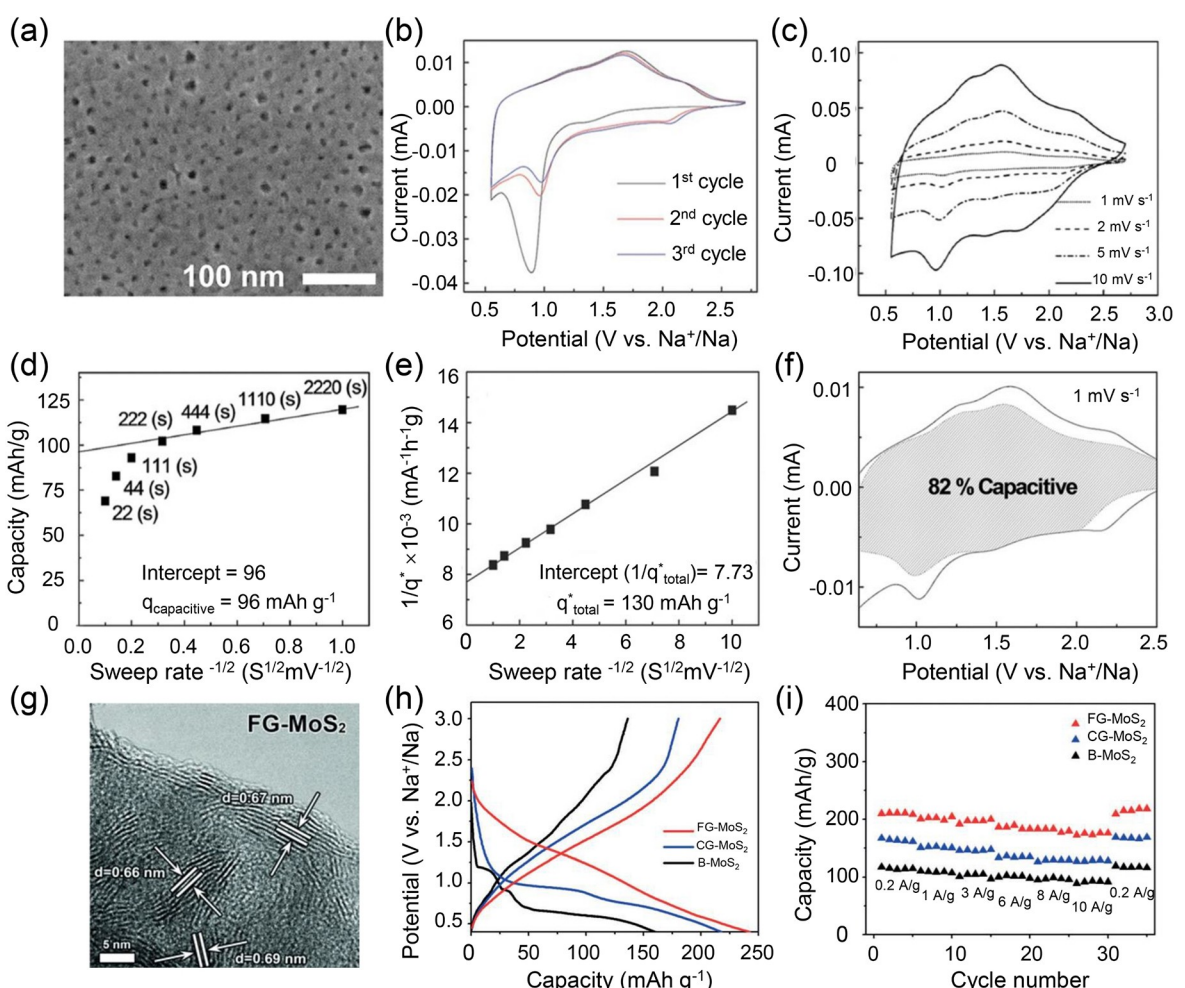


Figure 6. a) SEM image, b) initial CV curves at 5 mV s^{-1} , and c) CV curves at different sweep rates of mp-MoS₂, respectively. d) The calculated $q_{\text{capacitive}}$ and e) q_{total} according to the Trasatti analysis method, respectively. f) Capacitive and diffusion control contributions of mp-MoS₂ anode at 1 mV s^{-1} . Reprinted from Ref. [40] with permission, Copyright (2016) Wiley-VCH. g) TEM image of FG-MoS₂. h) The initial galvanostatic dis(charge) curves and i) rate performance of FG-MoS₂, CG-MoS₂, and B-MoS₂, respectively. Reprinted from Ref. [41] with permission, Copyright (2014) Wiley-VCH.

from 0.62 to 1 nm through heating-controlled deintercalation of NH₄⁺ ions, and found the MoS₂ with the *d*-spacing of 0.73 nm showed the most balanced electrochemical performance. Synergistically tuning the interplanar spacing, the number of layers, and the size of MoS₂ were investigated by Xu *et al.*^[42] Density functional theory (DFT) calculations illustrated that the diffusion of Na⁺ on the surface had a lower energy barrier of Na⁺ diffusion than in the interspace between two MoS₂ layers. Therefore, the ultrasmall MoS₂ nanosheets (US-MoS₂) performed the highly pseudocapacitive property. Growing MoS₂ nanosheets (NSs) on conductive graphene scaffolds was a useful strategy for providing fast electron transport networks and enhancing the rate performance.^[42] The highly orientated spatial geometry of MoS₂ was beneficial for shorting ion diffusion distances. The vertically oriented MoS₂ NSs on nitrogenous reduced graphene oxide (VO-MoS₂/N-RGO) provided efficiently shortened Na⁺ diffusion and electron transport length, and achieved excellent rate capability, a capacity of 153 mAh g⁻¹ at 20 A g⁻¹.^[91]

6. Transition Metal Carbides: MXenes

MXenes are the emerging pseudocapacitive materials for both aqueous and non-aqueous systems. MXenes are 2D transition metal carbides obtained by selectively etching A element from the MAX phases (where A is mainly a group IIIA or IVA).^[92-94] Usually, the formula of MXene is M_{n+1}X_nT_x (where M=transition metal such as Ti, V, Cr, Nb and so forth, X=carbon or nitrogen, T_x=surface functional termination group). MXenes are regarded as promising sodium-ion storage materials due to their characteristics of high electrical conductivity, large redox surface area, good hydrophilicity and so forth.^[95-97] Kajiyama *et al.* investigated the Na⁺ intercalation mechanism of Ti₃C₂T_x MXene NSs in the non-aqueous electrolyte (1 M NaPF₆ in EC/DEC, 1:1 by volume) through ex-situ XRD, TEM (Figure 7a), ²³Na magic angle spinning nuclear magnetic resonance (MAS NMR) (Figure 7b) and other analysis methods.^[98] Ex-situ XRD patterns of Ti₃C₂T_x (Figure 7a) showed the shift of (002) peak to a lower angle after the initial sodiation process. The ex-situ HRTEM images further confirmed that the expansion of interlayer space

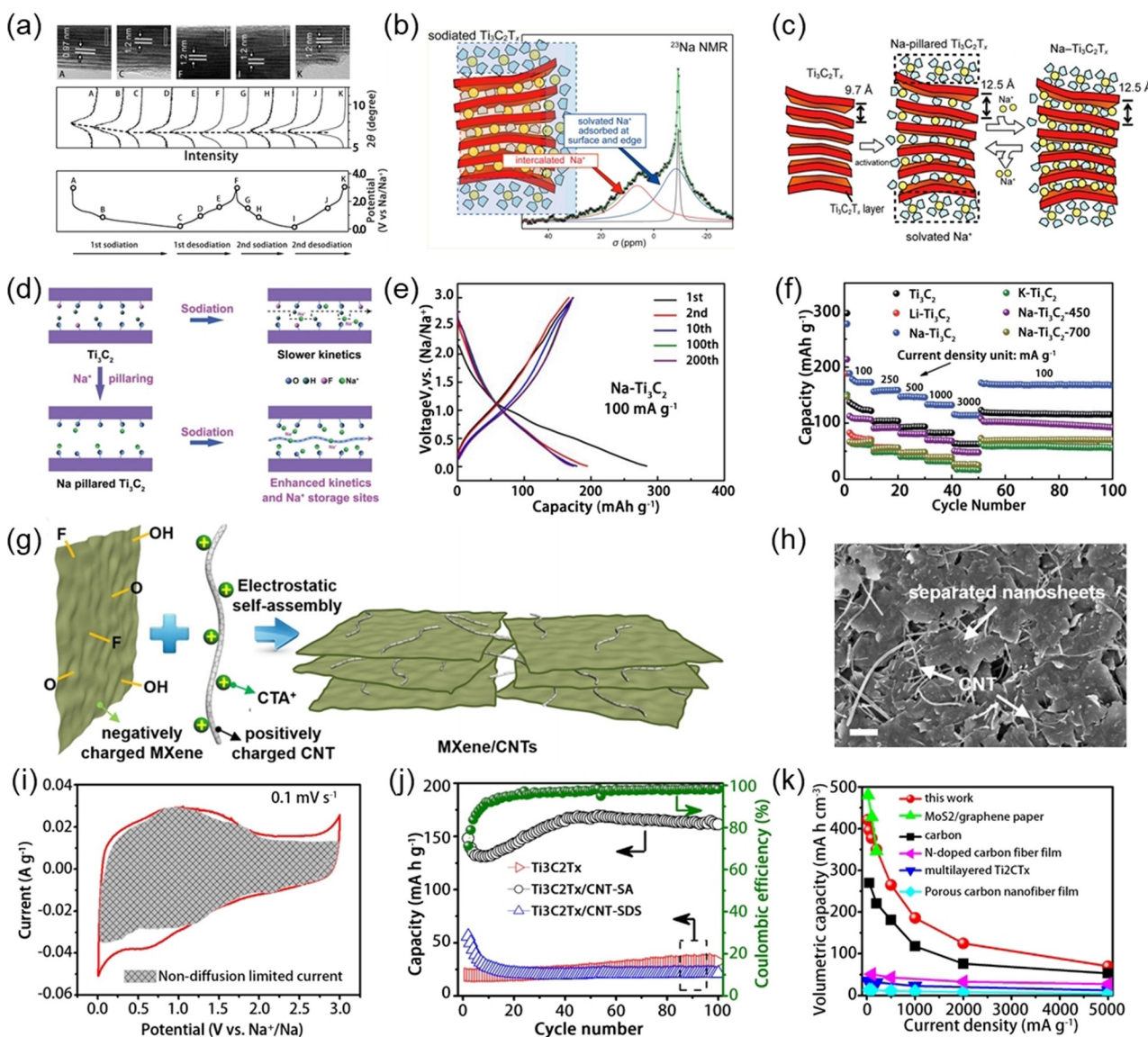


Figure 7. a) Ex situ XRD patterns and TEM images of Ti₃C₂T_x anode during sodiation and desodiation. b) ²³Na MAS NMR spectrum of sodiated Ti₃C₂T_x. c) Schematic of the proposed Na⁺ intercalation mechanism of Ti₃C₂T_x. Reprinted from Ref. [98] with permission, Copyright (2016) American Chemical Society. d) Schematic of the synthesis process of Na pillared Ti₃C₂ (Na-Ti₃C₂). e) The (dis)charge curves of Na-Ti₃C₂ at 100 mA g⁻¹. f) Rate performance of the different Ti₃C₂ MXene anodes. Reprinted from Ref. [69] with permission, Copyright (2018) Royal Society of Chemistry. g) Schematic of assembling porous MXene/CNT paper. h) SEM image of porous Ti₃C₂T_x/CNT-SA. i) Separation of the non-diffusion limited currents of the Ti₃C₂T_x/CNT-SA at 0.1 mV s⁻¹. j) Cycling performance of Ti₃C₂T_x/CNT papers at 20 mA g⁻¹. k) Volumetric capacities of Ti₃C₂T_x/CNT-SA and other reported electrode materials. Reprinted from Ref. [100] with permission, Copyright (2016) Elsevier.

from 9.7 to 12.5 Å after Na⁺ intercalation. It should be noted that the (002) peak change negligibly in the subsequent (dis)charge steps, indicating the very small “layered breathing” after the initial activation process. ²³Na MAS NMR is a useful technology to investigate the solvated environment of Na⁺ ions (Figure 7b). The sharp peak (at ~9 ppm) was the solvated Na⁺ from the residual electrolyte, the broad negative peak (at ~-8 ppm) might be from the solvated Na⁺ that trapped in SEI or absorbed at the external surface and the edge of particles. The broad positive peak (at +5 ppm) indicated the desolvated Na⁺ intercalated into Ti₃C₂T_x layers. By normalizing the NMR signal based on the area of broad negative peak, the broad positive peak increased during sodiation and decreased during

desodiation, which indicated that the sodium-ion storage process of Ti₃C₂T_x was mainly derived from desolvated Na⁺ intercalation. Figure 7c schematically summarized the sodium-ion storage mechanism of the Ti₃C₂T_x MXene. In the first sodiation process, solvated Na⁺ was absorbed on the electrode surface and accompanied with the decomposition of electrolyte and the formation of SEI layers. Simultaneously, desolvated Na⁺ with some of solvent molecules co-intercalated into Ti₃C₂T_x layers upon the initial sodiation step. The co-intercalation species acted as “pillars” to expand the interlayer spacing, which opened the Na⁺ intercalation channel and offered active sites. After the first activation process, the desolvated Na⁺ reversibly intercalated and extracted in between the expanded

$\text{Ti}_3\text{C}_2\text{T}_x$ layers without structural change, which was beneficial for high rate capability and cycling stability.

Based on the deep understanding of the sodium-ion storage mechanism for MXenes, expanding the interlayer space and maintaining their stability are important routes to achieve high-rate sodiation performance.^[37,39] One effective method was the pretreatment of MXenes by alkali metal ions to enlarge the spacing of layers.^[99] Luo *et al.* prepared a series of alkali metal ion pillared Ti_3C_2 (including $\text{Li}-\text{Ti}_3\text{C}_2$, $\text{Na}-\text{Ti}_3\text{C}_2$ and $\text{K}-\text{Ti}_3\text{C}_2$) and investigated their sodium-ion storage behavior and detailed reaction kinetics (Figure 7d).^[69] The interlayer spacing of the alkali metal ion pillared TiC_2 was $\sim 12.6 \text{ \AA}$, very close to the above mentioned 12.5 \AA that through an electrochemical activation by Na^+ intercalating into Ti_3C_2 (Figure 7a). The (dis)charge curves of $\text{Na}-\text{Ti}_3\text{C}_2$ (Figure 7e) displayed the slope line at a specific current of 100 mA g^{-1} , revealing the pseudocapacitive behavior. The $\text{Na}-\text{Ti}_3\text{C}_2$ anode displayed much enhanced rate performance (Figure 7f) and long-term cycling performance, owing to the more active sites and lower Na^+ diffusion barrier by Na^+ pillaring compared with those of Ti_3C_2 , $\text{Li}-\text{Ti}_3\text{C}_2$ and $\text{K}-\text{Ti}_3\text{C}_2$. Additionally, the $-\text{OH}$ terminal groups had the huge influence on their electrochemical performance. By annealing the samples at a high temperature (*e.g.* 450 and 700°C), the content of surface $-\text{OH}$ group was decreased. The specific capacity of $\text{Na}-\text{Ti}_3\text{C}-450$ and $\text{Na}-\text{Ti}_3\text{C}-750$ was lower than that of $\text{Na}-\text{Ti}_3\text{C}_2$, owing to the $-\text{OH}$ terminal group was beneficial for enlarging the interlayer distance and increasing the number of active sites.

The gravimetric capacity is usually regarded as a critical index to evaluate the performance of electrode materials. However, for portable and wearable devices, the volumetric capacity needs more attention.^[38,99] Xie *et al.* reported the MXene/CNT composite paper electrode with high volumetric capacity.^[100] This paper electrode was prepared by electrostatic self-assembly between negative charge of 2D $\text{Ti}_3\text{C}_2\text{T}_x$ NSs and positively charge of cetyltrimethylammonium bromide (CTAB) modified one dimensional (1D) CNTs (Figure 7g), named as $\text{Ti}_3\text{C}_2\text{T}_x/\text{CNT-SA}$. The $\text{Ti}_3\text{C}_2\text{T}_x/\text{CNT-SA}$ paper had a density of 2.4 g cm^{-3} . The CNTs not only enhanced the electrical conductivity of electrodes but also inhibited the aggregation of $\text{Ti}_3\text{C}_2\text{T}_x$ NSs. The heterostructure paper with porosity ensured the specific surface area of the active materials and the accessibility of electrolytes. SEM image (Figure 7h) showed the uniformly separated $\text{Ti}_3\text{C}_2\text{T}_x$ NSs by CNTs, which effectively prevented the restack of $\text{Ti}_3\text{C}_2\text{T}_x$ NSs and formed a conductive network for fast electron transport. The CV curve (Figure 7i) displayed a rectangle shape with broad cathodic/anodic peaks at $\sim 0.6/1.0 \text{ V}$. According to the quantitative analysis, the shaded area corresponding to the capacitive contribution occupied 88.1% of total capacity at 0.1 mV s^{-1} , indicating a non-diffusion capacitive-dominated sodium-ion storage process. This $\text{Ti}_3\text{C}_2\text{T}_x/\text{CNT-SA}$ paper exhibited much enlarged capacity and cycling stability than pure $\text{Ti}_3\text{C}_2\text{T}_x$ and $\text{Ti}_3\text{C}_2\text{T}_x/\text{CNT-SDS}$ (restacked $\text{Ti}_3\text{C}_2\text{T}_x$ layers). It was worth highlighting that $\text{Ti}_3\text{C}_2\text{T}_x/\text{CNT-SA}$ exhibited a high volumetric capacity of characteristic 421 mAh cm^{-3} at 20 mA g^{-1} and 89 mAh cm^{-3} at even up to 5000 mA g^{-1} (Figure 7j). The outstanding volumetric

capacities performance exceeded other reported electrode materials (Figure 7k).

Various modified methods have been developed to tune the interlayer spacing and surface functional groups of MXenes to optimize the sodium-ion storage performance. However, the ICE of MXene for sodium-ion storage is still very low, and there is no doubt that it should be enlarged soon. Besides, the detailed influences of the surface functional group for electrochemical performance and the formation of SEI layers are unclear. Most of the MXenes are currently synthesized by selective etching in aqueous HF, which contains surface functional groups (*e.g.* $-\text{O}$, $-\text{OH}$, $-\text{F}$). Recently, the Lewis acidic etching routes were developed to effectively synthesize new MXenes, and tune the surface chemistry of MXene materials. Li *et al.* showed the remarkable pseudocapacitive Li^+ ion storage performance of the molten salt synthesized Ti_3C_2 MXene. The universal methods to synthesize much high-performance MXene are advisable.

7. Transition Metal Nitrides and Phosphides

Transition metal nitrides have superior electronic conductivity, thermostability and excellent hardness, which are regarded as promising active materials for electrochemical storage.^[101,102] Except for the high electronic conductive but expensive $\text{RuO}_2 \cdot n\text{H}_2\text{O}$, transition metal nitrides have exhibited high pseudocapacitance in aqueous electrolyte.^[103,104] Meanwhile, they display promising electrochemical performance for lithium-ion and sodium-ion storage in non-aqueous electrolyte as well, but the detailed stored capacities are quite different. For example, the Sn_3N_4 anode material delivered the reversible lithiation capacity of $\sim 1500 \text{ mAh g}^{-1}$ at 100 mA g^{-1} , but the related sodiation capacity was only $\sim 190 \text{ mAh g}^{-1}$ at the same (dis)charge current.^[105] Similar phenomena was observed in VN anode: a lithiation capacity of 365 mAh g^{-1} at 0.2 C , but only a sodiation capacity of 90 mAh g^{-1} .^[106] According to the storage mechanism based on conversion reaction, *e.g.* Sn_3N_4 experimental results showed inconsistent data, which meant the storage mechanism of sodium-ion might be different from that of lithium-ion. Additionally, if they followed the traditional ion intercalation reaction mechanism, the charge stored capacity was not critical for their particle size. But, it was found that the different nanosized VN and Mo_3N_2 grains delivered the specific capacity which was largely dependent on their specific surface area.^[107] The sodium-ion storage mechanism of transition metal nitrides might be much more complex and needed to be further understood.

Usually, the amorphous oxide layers were detected on the surface of various transition metal nitrides, when they were exposed to air (or oxygen) atmosphere or an uncompleted anion exchange process during annealing in ammonia flow.^[43] As known, the surface oxides exhibited the merit of electrochemical activity, which might contribute to the sodium-ion storage capability. One rational sodium-ion storage mechanism of transition metal nitrides was proposed (Figure 8a), that was the surface oxides on the transition metal nitrides reacted with

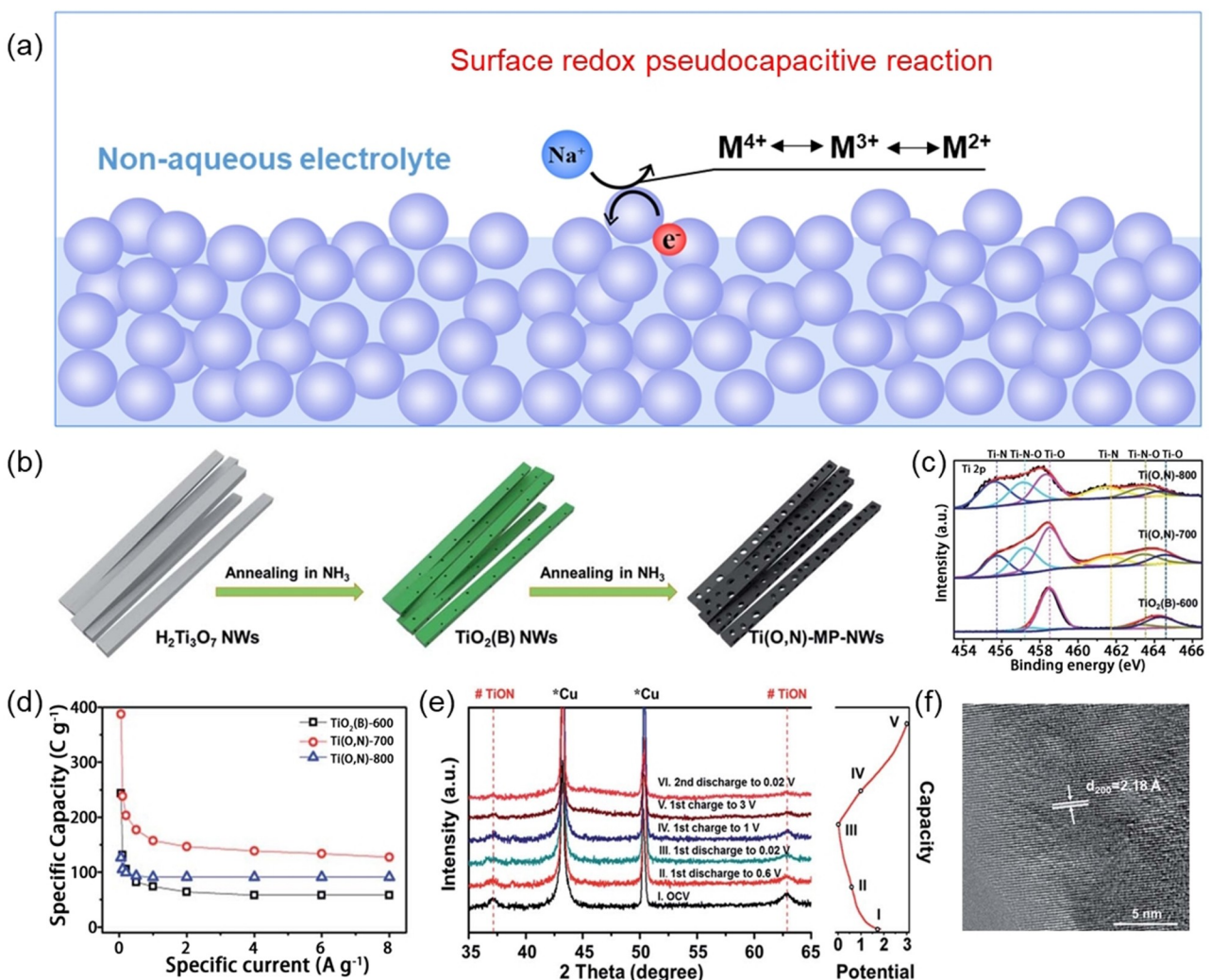


Figure 8. a) Schematic of the surface redox pseudocapacitive sodium-ion storage mechanism. Reproduced from Ref. [107] with permission, Copyright (2020) Elsevier. b) Schematic of the synthesis of titanium oxynitride mesoporous nanowires. c) XPS spectra of Ti 2p and d) rate performance of TiO₂(B)-600, Ti(O,N)-700 and Ti(O,N)-800, respectively. e) Ex-situ XRD patterns at different (dis)charge states and f) HRTEM image at discharged to 0.02 V of Ti(O,N)-700 electrode, respectively. Reprinted from Ref. [43] with permission, Copyright (2017) Royal Society of Chemistry.

Na⁺ and the inner transition metal nitrides might be unreacted.^[43,107,108] The ultrathin layer of surface oxides provided a very short ion diffusion distance and the fast reversible redox reaction, showing the surface pseudocapacitive charge storage processes.

Dong *et al.* investigated the sodium-ion storage mechanism and electrochemical performance of titanium nitride.^[43] The hydrogen titanate (H₂Ti₃O₇) NWs were used as the precursor and transformed into titanium nitride by annealing under ammonia flow at different temperatures, named as Ti(O,N)-700 and Ti(O,N)-800 (Figure 8b). The X-ray photoelectron spectroscopy (XPS) of Ti 2p spectra (Figure 8c) demonstrated the existence of the surface oxides (Ti—N—O and Ti—O peaks) with the +4 valence of titanium. The relative ratio of Ti—O peak for Ti(O,N)-700 was stronger compared with that of Ti(O,N)-800, indicating the more oxygen residue when annealing at low temperature. The Brunauer-Emmett-Teller (BET) surface area of TiO₂(B)-600, Ti(O,N)-700, Ti(O,N)-800 were 29.02, 49.25 and

70.75 m²g⁻¹, respectively. But, the Ti(O,N)-700 delivered a specific capacity of 387 Cg⁻¹ at 0.05 Ag⁻¹ (Figure 8d), which was much higher than that of Ti(O,N)-800 (92 Cg⁻¹) and TiO₂(B)-600 (58 Cg⁻¹). These indicated a surface-depended charge storage reaction of Ti(O,N). The Ti(O,N)-700 anode displayed excellent rate capability (Figure 8d) and cycling stability. Ex-situ XRD patterns (Figure 8e) of Ti(O,N)-700 at various (de)sodiated states showed diffraction peak without obvious shift or change compared with the pristine state, indicating no phase transformation of crystalline TiN structure. TEM image of Ti(O,N)-700 at a totally sodiated state (Figure 8f) displayed the lattice fringe of d_{200} (2.18 Å). The quantitative analysis demonstrated the capacitive dominated charge storage. The above unchanged Ti(O,N) crystal during (de)sodiation might indicate an intercalation reaction without phase changes or surface redox pseudocapacitance from the surface amorphous oxides. But, the surface-depended specific capacity (Figure 8d) supported the mechanism that was a surface-redox

pseudocapacitance (Figure 8a). Besides, the Mo_3N_2 was followed the surface-redox pseudocapacitive sodiation as well.^[107]

Similar to nitrides, transition metal phosphides with high electronic conductivity are considered promising electrode materials.^[108,109] It was inferred that the surface-redox pseudocapacitive sodium-ion storage also occurs at phosphides. Jiang *et al.* investigated the sodium-ion storage mechanism of MoP.^[44] The MoP NPs/carbon NWs composites were synthesized by annealing the $\text{Mo}_3\text{O}_{10}(\text{C}_6\text{H}_8\text{N})_2 \cdot 2\text{H}_2\text{O}$ NWs under ammonia flow at 700 °C for 3, 13 and 24 hours, named as MoP/C-3 h, 13 h, and 24 h, respectively (Figure 9a). The Mo 3d spectra

(Figure 9b) showed the divisive peaks for the MoP (Mo^{3+}) and the surface molybdenum oxides with high oxidation states (Mo^{4+} and Mo^{6+}). According to the fitting results, the content of $\text{Mo}^{6+}/\text{Mo}^{4+}$ in MoP/C-3 h was 60.2%, which was higher than that of MoP/C-13 h (54.6%) and MoP/C-24 h (27.3%). Interestingly, the in-situ XRD patterns of MoP/C-3 h and corresponding (dis)charge curves in the first two cycles were shown in Figure 9c. It should be noted that the sodiation and desodiation processes were highly reversible, while the crystal structure of MoP almost remained unchanged. The morphology of mesoporous NWs and *d*-spacing of MoP crystalline (Figure 9d–

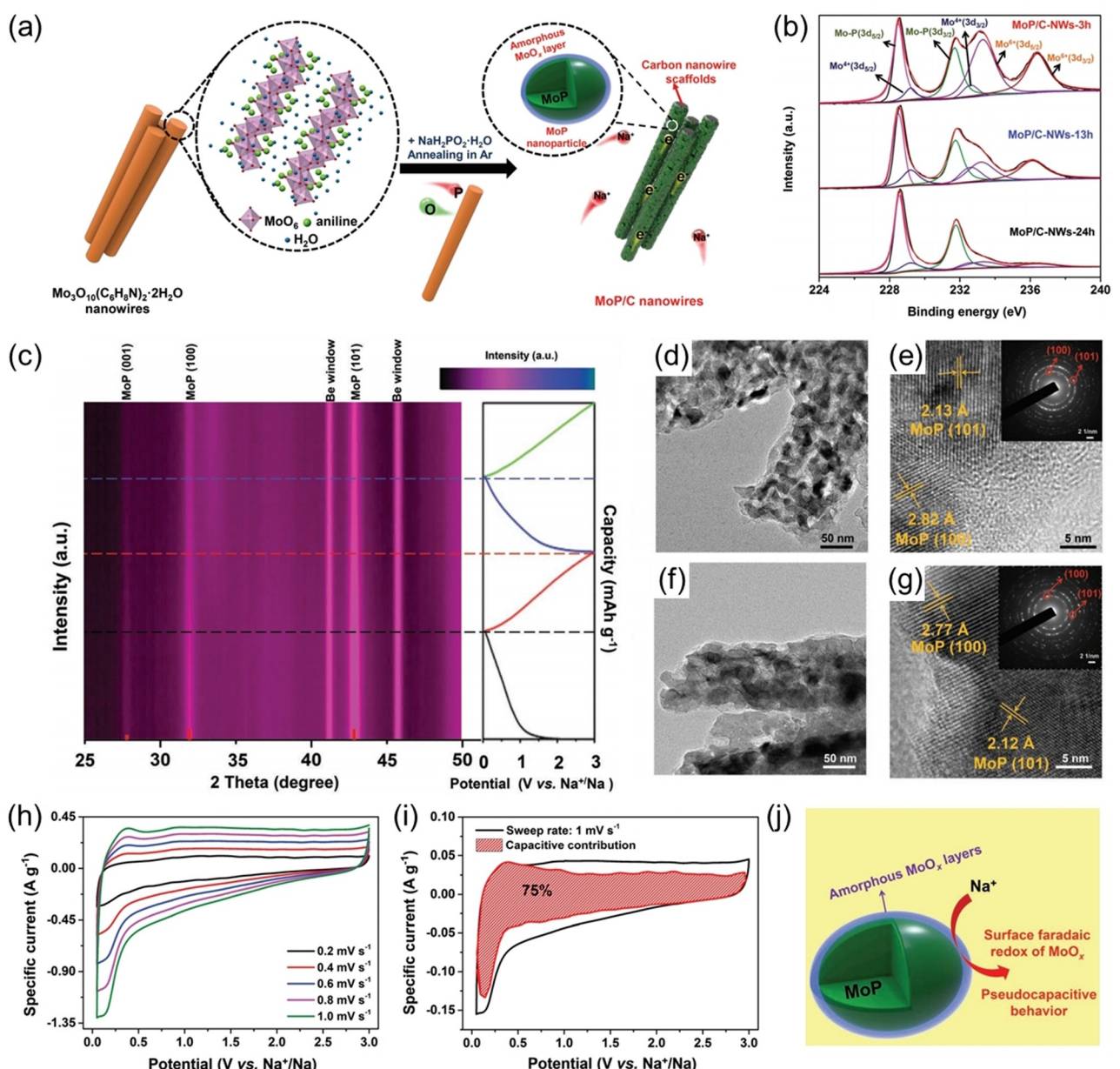


Figure 9. a) Schematic of the synthesis process of MoP/C mesoporous NWs. b) Mo 3d XPS spectra of MoP/C-3 h, -13 h, and -24 h. c) *In situ* XRD patterns of MoP/C-3 h at the first two cycles. d) Ex-situ TEM image, e) HRTEM image, and SAED pattern (inset of e) of MoP/C-3 h at fully sodiated state, respectively. f) TEM image, g) HRTEM image, and SAED pattern (inset of g) of MoP/C-3 h at fully desodiated state, respectively. h) CV curves of MoP/C-3 h at different sweep rates. i) CV curves of MoP/C-3 h at 1.0 mVs⁻¹, while the shaded areas showing the capacitive controlled regions. j) Schematic of sodium-ion storage mechanism for the MoP. Reprinted from Ref. [44] with permission, Copyright (2021) Wiley-VCH.

g) remained pretty well at the sodiated and desodiated states. The galvanostatic (dis)charge curves of MoP/C-3 h exhibited the pseudocapacitance-like sodium-ion storage behavior. The ICE was 77.3%. The CV curves of MoP/C-3 h at various sweep rates (Figure 9h) showed the pseudocapacitive box-like shape and negligible change with the increase of sweep rates, indicating excellent rate performance. A quantitative analysis was calculated (Figure 9i) that ~75% of the total stored charge was dominated by the capacitive response at a low sweep rate of 1 mV s^{-1} . As discussed above, similarly to that of $\text{Ti(O,N)}^{[43]}$ and $\text{Mo}_3\text{N}_2^{[107]}$ the sodium-ion storage of MoP was a surface faradaic redox pseudocapacitive reaction derived from the molybdenum oxides layers on the MoP (Figure 9j). Therefore, the MoP/C-3 h with rich surface oxides exhibited much enhanced specific capacity (293 mAh g^{-1} at 0.1 A g^{-1}) than that of MoP/C-13 h (269 mAh g^{-1}) and MoP/C-24 h (169 mAh g^{-1}) and rate capability (71 mAh g^{-1} at 20 A g^{-1}). This surface-redox pseudocapacitive material showed high cycling stability as well.

8. Assembly of Advanced Sodium-Ion Capacitors

Generally, similar to the construction of LIC, the SICs are asymmetric electrochemical capacitors as well. It could be assembled by coupling the battery-type negative electrode with EDLC-type positive electrode, herein, named as battery-EDLC hybrid SIC. In this case, through the utilization of faradaic battery-type anode with much enhanced specific capacity and lower operation potential, the overall capacity, operating voltage, and thus energy density of battery-EDLC hybrid SIC are much improved than those of EDLCs.^[110,111] However, the rate capability of this SIC is very dependent on the battery-type anode which follows the semi-diffusion control process.

The reaction kinetics between positive and negative electrodes of SICs could be matched through the use of high-rate pseudocapacitive anode materials coupled with the EDLC-type positive materials, named as pseudocapacitor-EDLC hybrid SIC (Figure 10a). Table 1 and 2 summarize the electrochemical

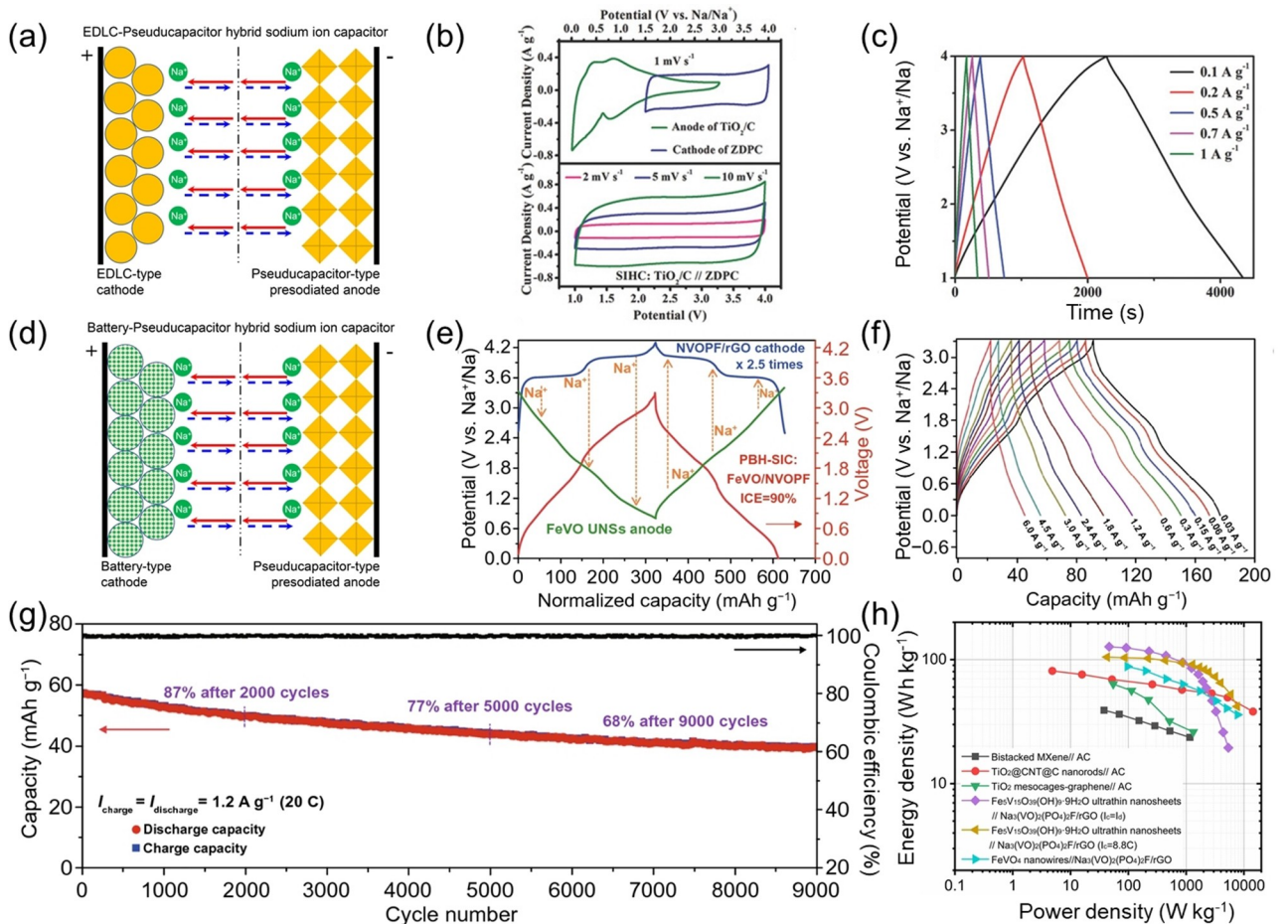


Figure 10. a) Schematic of EDLC-pseudocapacitor hybrid sodium-ion capacitor. b) The CV curves of TiO_2/C anode, 3D nanoporous carbon (ZDPC) cathode and the $\text{TiO}_2/\text{//ZDPC}$ hybrid device. c) The (dis)charge curves of $\text{TiO}_2/\text{//ZDPC}$ hybrid device. (b) and (c) are reprinted from Ref. [45] with permission, Copyright (2018) Wiley-VCH. d) Schematic of pseudocapacitor-battery hybrid sodium-ion capacitor. e) The (dis)charge curves of FeVO UNSs anode, NVOPF/rGO cathode and the FeVO//NVOPF hybrid sodium-ion capacitor. f) Rate performance and g) cycling performance of FeVO//NVOPF hybrid sodium-ion capacitor. (e)–(g) are reprinted from Ref. [46] with permission, Copyright (2021) The Authors. h) The summary of energy density vs. power density of the hybrid devices listed in Table 2.

SICs	Anode Material	Cathode Material	Mass ratio (N:P)	Electrolyte	Additional treatment	Voltage window [V]	Energy density at power density ^[a]	Cycling performance	Ref.
Pseudocapacitor-EDLC hybrid SIC	bistacked $\text{Ti}_3\text{C}_2\text{T}_x/\text{d-Ti}_3\text{C}_2\text{T}_x$ MXene	Activated carbon	1:1.2	1 M NaClO ₄ EC _{37.5} ; PC _{47.5} ; FEC ₅	presodiation	0.6–4.0	39 Wh kg ⁻¹ at 0.02 kW kg ⁻¹ 23 Wh kg ⁻¹ at 1.14 kW kg ⁻¹	84.22% after 4000 cycles at 20 mV s ⁻¹	[112]
	TiO ₂ meso-cages-graphene	Activated carbon	1:5	1 M NaClO ₄ EC ₃₀ ; PC ₃₀ ; FEC ₅	presodiation	1.0–3.8	64.2 Wh kg ⁻¹ at 0.056 kW kg ⁻¹ 25.8 Wh kg ⁻¹ at 1.357 kW kg ⁻¹	90% after 10000 cycles at 10 °C	[116]
	TiO ₂ @CNT@C nanorods	Biomass-derived carbon	1:3	1 M NaClO ₄ EC ₃₀ ; PC ₃₀	presodiation	1.0–4.0	81.2 Wh kg ⁻¹ at 0.126 kW kg ⁻¹ 37.9 Wh kg ⁻¹ at 12.4 kW	85.3% after 5000 cycles at 1 A g ⁻¹	[117]
Pseudocapacitor-battery hybrid SIC	MXene Ti_2CT_x	$\text{Na}_2\text{Fe}_2(\text{SO}_4)_3$	1:4	1 M NaPF ₆ EC ₃₀ ; DEC ₃₀	no	0.1–3.8	64 Wh kg ⁻¹ at 0.072 kW kg ⁻¹ 52 Wh kg ⁻¹ at 0.288 kW kg ⁻¹	96% after 100 cycles at 0.6 A g ⁻¹	[118]
	FeVO UNSs	NVOPF/rGO	1:2.5	1 M NaPF ₆ DEGDME	no	0–3.3	126 Wh kg ⁻¹ at 0.091 kW kg ⁻¹ 43 Wh kg ⁻¹ at 7.6 kW kg ⁻¹	68% after 9000 cycles at 1.2 A g ⁻¹	[46]
	FeVO ₄ ·nH ₂ O NWs	NVOPF/rGO	1:2	1 M NaPF ₆ DEGDME	no	0.4–3.2	88 Wh kg ⁻¹ at 0.095 kW kg ⁻¹ 35 Wh kg ⁻¹ at 7.9 kW kg ⁻¹	60% after 5000 cycles at 1 A g ⁻¹	[83]

[a] The energy density and power density were calculated based on the total mass of cathode and anode active materials.

performance of reported pseudocapacitive sodium-ion anode materials and hybrid SICs, respectively. Kurra *et al.* assembled the pseudocapacitive bistacked $\text{Ti}_3\text{C}_2\text{T}_x/\text{d-Ti}_3\text{C}_2\text{T}_x$ MXene//AC hybrid SICs,^[112] which delivered an energy density of 39 Wh kg⁻¹ at a power density of ~0.02 kW kg⁻¹, 23 Wh kg⁻¹ at 1.14 kW kg⁻¹, and the capacity retention of 84.22% after 4000 cycles in the voltage range of 0.6–4.0 V. Consisting of pseudocapacitive TiO₂/C anode and MOF-derived three dimensional (3D) nanoporous carbon cathode, the hybrid SIC operated in 1.0–4.0 V showed box shape CV curves at different sweep rates (Figure 10b) and slope-like (dis)charge profiles at each specific currents (Figure 10c).^[45] It achieved the maximum energy density of 142.7 Wh kg⁻¹ at 0.25 kW kg⁻¹ and the high energy density of 61.8 Wh kg⁻¹ at the high-power of 25 kW kg⁻¹. This hybrid device performed the capacity retention of 90% after 10,000 cycles at 1 A g⁻¹. The EDLC-type positive material and the battery-type or pseudocapacitive anode material did not provide Na⁺ ions. Meanwhile, at present, most of the battery-type or pseudocapacitive anode materials exhibited low ICE owing to the electrolyte decomposition, SEI layer formation, and irreversible phase transition of the anode materials in the initial sodiation process. Thus, it is usually needed the additional pre-sodiation step before assembling into SIC.

Sodium-rich battery-type cathode materials could provide the extracted Na⁺ that diffused into the pseudocapacitive anode, which could waive the complex pre-sodiation process for the assemble pseudocapacitor-battery of hybrid SIC (Figure 10d). This requires the battery-type cathode materials to operate at high potential and deliver excellent high-rate capability. The NASCIOn-type Na₃V₂(PO₄)₃,^[91] and layered Na₃(VO)₂(PO₄)₂F (NVOPF)^[46,83] cathode delivered ultrahigh rate capability up to 200 C, which were promising candidates. The pseudocapacitive anode materials, such as FeVO₄·nH₂O NWs and FeVO UNSs, delivered very high ICE, high specific capacity and high-rate capability.^[46,83] Figure 10e shows the operating mechanism of the FeVO UNSs//NVOPF hybrid SIC.^[46] The Na⁺ extracted from NVOPF cathode then inserted into FeVO UNS anode during the charging process, then, it moved contrary during discharging step. The assembled FeVO UNSs//NVOPF hybrid SIC showed a high ICE of ~90%. The galvanostatic (dis)charge curves of the NVOPF//FeVO PBH-SIC showed capacitive quasi-linear slopes at different high specific currents in 0–3.3 V (Figure 10f). The well-assembled FeVO UNSs//NVOPF hybrid SIC displayed a capacity retention of 68% after 9000 cycles at 20 C. The FeVO UNSs//NVOPF-rGO hybrid SIC delivered a high energy density of 126 Wh kg⁻¹ at 0.091 kW kg⁻¹, and 43 Wh kg⁻¹ at 7.6 kW kg⁻¹ (Figure 10h).^[46] The assembled FeVO₄·nH₂O//Na₃(VO)₂(PO₄)₂F-rGO delivered an energy density of 88 Wh kg⁻¹ at 0.095 kW kg⁻¹ and a high power density of 7.9 kW kg⁻¹ with the energy density of 35 Wh kg⁻¹, and the capacity retention of 60% after 5000 cycles.^[83] The pseudocapacitive FeVO₄·nH₂O and FeVO UNSs anode operated in a very safe potential range, enabling a high safety of SIC at high rates. The pseudocapacitor-battery hybrid sodium-ion capacitors use both faradaic cathode and anode, delivering enhanced energy density than those of only using EDLC-type cathode (Figure 10h). The

application of pseudocapacitive materials promotes the development of SICs toward achieving both high energy and high power densities.

9. Conclusions and Outlook

Pseudocapacitive materials deliver both high specific capacity and high-rate capability (finishing a charge or discharge in minutes). These materials realize the high-rate sodium-ion storage with small potential hysteresis, while the bulk battery-type materials suffer from sluggish kinetics of Na^+ diffusion and huge overpotentials (Figure 1). Herein, we review the electrochemical features and performance of pseudocapacitive sodium-ion storage anode materials reported in recent years. As summarized in Table 1 and Figure 11,^[9] the pseudocapacitive anode materials deliver excellent ultrahigh rate performance even at the high rates up to 30 C. For example, the TiO_2 anode materials displayed a high specific capacity of 248 mAh g^{-1} at 0.1 A g^{-1} , 160 mAh g^{-1} (64.5% of state of charge (SOC)) at 4 A g^{-1} (corresponding to the (dis)charge time of 2.4 min), and ~30% of SOC finished in 13.2 seconds (at 20 A g^{-1}). The FeVO UNSs anode delivered 290 mAh g^{-1} at 0.1 A g^{-1} , 175 mAh g^{-1} (60.3% of SOC) at 6 A g^{-1} (in 1.75 minutes), and 80 mAh g^{-1} (27.6% of SOC) in 14.4 seconds. Further, the assembled SICs through coupling the pseudocapacitive anode materials with the EDLC-type or battery-type cathode materials deliver high energy density at high power density (Table 2).

The pseudocapacitive sodium-ion storage materials are emerging and remain largely unexplored. Several future directions and challenges are proposed as follows.

Figure out the relationships among the storage mechanism, structure/morphology, and electrochemical performance of pseudocapacitive materials. This is important for effectively

optimizing their comprehensive performance. The specific capacity of surface redox pseudocapacitive materials depends on their surface areas. Some battery-type materials exhibit pseudocapacitive behavior by reducing their grain sizes into several nanometers, thus, whose charge storage feature becomes a surface-dominant capacitive process. These unique active materials are called as extrinsic pseudocapacitive materials.^[9,26] There is lacking clear boundaries among the surface-redox pseudocapacitive, intercalation pseudocapacitive and extrinsic pseudocapacitive materials. Further works are encouraged to revealing these relationships and understanding the insight sodium-ion storage mechanisms of pseudocapacitive materials.

At present, the electrochemical performance of pseudocapacitive sodium-ion materials is mostly investigated based on low mass loadings or thin-film electrodes, in which the ion diffusion and electron transport kinetics are largely enhanced. To promote practical applications, realizing the rapid reaction kinetics of pseudocapacitive electrode at high mass loading level is necessary. As known, the thickness of electrodes relies on the packing density of active materials. The designs of order and secondary assembled nanostructures that ensure large electrode-electrolyte contact area and high density are necessary. The layer-by-layer assemble of nanomaterials and conducive matrices,^[113] and the synthesis of large-sized mesoporous materials with controlled porosity that enable efficient electrolyte diffusion are able to achieve high packing density of electrode materials.

The initial and subsequent coulombic efficiency of pseudocapacitive anode materials should be taken into considerations seriously. The requirement for the cycling life of capacitors is ten or hundred times longer than that of batteries, therefore the coulombic efficiency should be pretty high. Future works need to focus on the insight surface/interface chemistry of pseudocapacitive materials, such as understanding the composition and microstructure of SEI layers and the related influence on their electrochemical performance. Development of new electrolyte systems with wide and stable operation potential window, high ionic conductivity, thin and stable SEI layers are needed. Theoretical computation will help screen the suitable solute and solvent of electrolytes with the formation of high-quality interfaces.

The SICs are a new kind of EES device. Nowadays, the reports of SICs are mostly lab-assembled coin cells. Assembling the prototypes of SICs in columnar or pouch cells with high mass loading of active materials is important, which helps to evaluate the electrochemical performance in the actual conditions. There have not mature pre-sodiation technologies up to now. The in-situ pre-sodiation strategy that uses organic or inorganic sodium salts cathode as extra Na^+ ion sources shows advantages to simplify the assembling processes of SICs,^[114] while the influence of irreversible by-products remains on the cathode sides needs further analysis. Instead of using EDLC-type high-area carbon-based cathode, the SICs consisted of Na-rich batter-type cathode materials and pseudocapacitive anode are easily assembled and show much higher energy density.^[46,83] The next-generation SICs could use hybrid

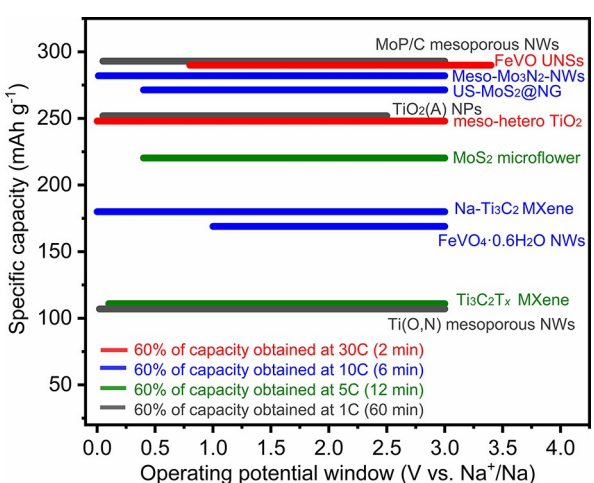


Figure 11. The electrochemical performance of reported state-of-the-art pseudocapacitive sodium-ion storage anode materials: MoP/C mesoporous NWs^[44], FeVO UNSs,^[46] meso-Mo₃N₂-NWs,^[107] US-MoS₂-NSs @NG,^[42] TiO₂ (A) NPs,^[75] meso-hetero-TiO₂,^[66] MoS₂ microflower,^[113] Na-Ti₃C₂ MXene,^[69] FeVO₄·0.6H₂O NWs,^[83] Ti₃C₂T_x MXene,^[96] and Ti(O,N) mesoporous NWs.^[43]

cathode (a composition of high-rate Na-rich batter-type cathode and high-surface-area carbon materials) and the high-performance pseudocapacitive anode, that simultaneously deliver high energy and power densities.

Acknowledgements

This work was supported by the National Natural Science Foundation of China (No. 22005256), the Natural Science Foundation of Fujian Province of China (No. 2020J01034), and the XMU Training Program of Innovation and Entrepreneurship for Undergraduates (No. 2020X750).

Conflict of Interest

The authors declare no conflict of interest.

Keywords: sodium-ion capacitors • pseudocapacitance • anode materials • hybrid capacitors • high power device

- [1] D. Larcher, J. M. Tarascon, *Nat. Chem.* **2015**, *7*, 19–29.
- [2] Z. Yang, J. Zhang, M. C. W. Kintner-Meyer, X. Lu, D. Choi, J. P. Lemmon, J. Liu, *Chem. Rev.* **2011**, *111*, 3577–3613.
- [3] D. M. Davies, M. G. Verde, O. Mnyshenko, Y. R. Chen, R. Rajeev, Y. S. Meng, G. Elliott, *Nat. Energy* **2019**, *4*, 42–50.
- [4] P. Simon, Y. Gogotsi, *Nat. Mater.* **2020**, *19*, 1151–1163.
- [5] Z. P. Cano, D. Banham, S. Ye, A. Hintennach, J. Lu, M. Fowler, Z. Chen, *Nat. Energy* **2018**, *3*, 279–289.
- [6] J. W. Choi, D. Aurbach, *Nat. Rev. Mater.* **2016**, *1*, 16013.
- [7] M. Salanne, B. Rotenberg, K. Naoi, K. Kaneko, P. L. Taberna, C. P. Grey, B. Dunn, P. Simon, *Nat. Energy* **2016**, *1*, 16070.
- [8] J. R. Miller, P. Simon, *Science* **2008**, *321*, 651.
- [9] C. Choi, D. S. Ashby, D. M. Butts, R. H. DeBlock, Q. Wei, J. Lau, B. Dunn, *Nat. Rev. Mater.* **2020**, *5*, 5–19.
- [10] D. P. Dubal, O. Ayyad, V. Ruiz, P. Gómez-Romero, *Chem. Soc. Rev.* **2015**, *44*, 1777–1790.
- [11] V. Aravindan, J. Gnanaraj, Y.-S. Lee, S. Madhavi, *Chem. Rev.* **2014**, *114*, 11619–11635.
- [12] P. Ruschhaupt, S. Pohlmann, A. Varzi, S. Passerini, *Batteries & Supercaps* **2020**, *3*, 698–707.
- [13] W. Zuo, R. Li, C. Zhou, Y. Li, J. Xia, J. Liu, *Adv. Sci.* **2017**, *4*, 1600539.
- [14] V. Aravindan, D. Mhamane, W. C. Ling, S. Ogale, S. Madhavi, *ChemSusChem* **2013**, *6*, 2240–2244.
- [15] J. Ding, W. Hu, E. Paek, D. Mitlin, *Chem. Rev.* **2018**, *118*, 6457–6498.
- [16] S. S. Zhang, *Batteries & Supercaps* **2020**, *3*, 1137–1146.
- [17] Y. Huang, L. Zhao, L. Li, M. Xie, F. Wu, R. Chen, *Adv. Mater.* **2019**, *31*, 1808393.
- [18] Y. Xiao, S. H. Lee, Y.-K. Sun, *Adv. Energy Mater.* **2017**, *7*, 1601329.
- [19] J.-Y. Hwang, S.-T. Myung, Y.-K. Sun, *Chem. Soc. Rev.* **2017**, *46*, 3529–3614.
- [20] C. Vaalma, D. Buchholz, M. Weil, S. Passerini, *Nat. Rev. Mater.* **2018**, *3*, 18013.
- [21] K. M. Abraham, *ACS Energy Lett.* **2020**, *5*, 3544–3547.
- [22] Q. Wei, R. H. DeBlock, D. M. Butts, C. Choi, B. Dunn, *Energy Environ. Mater.* **2020**, *3*, 221–234.
- [23] D. Kundu, E. Talaie, V. Duffort, L. F. Nazar, *Angew. Chem. Int. Ed.* **2015**, *54*, 3431–3448.
- [24] J. Deng, W.-B. Luo, S.-L. Chou, H.-K. Liu, S.-X. Dou, *Adv. Energy Mater.* **2018**, *8*, 1701428.
- [25] Y. Zhang, J. Jiang, Y. An, L. Wu, H. Dou, J. Zhang, Y. Zhang, S. Wu, M. Dong, X. Zhang, Z. Guo, *ChemSusChem* **2020**, *13*, 2522–2539.
- [26] V. Augustyn, P. Simon, B. Dunn, *Energy Environ. Sci.* **2014**, *7*, 1597–1614.
- [27] J. Wang, S. Dong, B. Ding, Y. Wang, X. Hao, H. Dou, Y. Xia, X. Zhang, *Natl. Sci. Rev.* **2017**, *4*, 71–90.
- [28] Y. Jiang, J. Liu, *Energy Environ. Mater.* **2019**, *2*, 30–37.
- [29] V. Augustyn, J. Come, M. A. Lowe, J. W. Kim, P.-L. Taberna, S. H. Tolbert, H. D. Abruna, P. Simon, B. Dunn, *Nat. Mater.* **2013**, *12*, 518–522.
- [30] R. Sun, Q. Wei, J. Sheng, C. Shi, Q. An, S. Liu, L. Mai, *Nano Energy* **2017**, *35*, 396–404.
- [31] T. Jin, H. Li, Y. Li, L. Jiao, J. Chen, *Nano Energy* **2018**, *50*, 462–467.
- [32] N. Liu, X. Wu, L. Fan, S. Gong, Z. Guo, A. Chen, C. Zhao, Y. Mao, N. Zhang, K. Sun, *Adv. Mater.* **2020**, *32*, 1908420.
- [33] L. Kong, C. Zhang, S. Zhang, J. Wang, R. Cai, C. Lv, W. Qiao, L. Ling, D. Long, *J. Mater. Chem. A* **2014**, *2*, 17962–17970.
- [34] J. Wang, J. Polleux, J. Lim, B. Dunn, *J. Phys. Chem. C* **2007**, *111*, 14925–14931.
- [35] M. Zukalová, M. Kalbáč, L. Kavan, I. Exnar, M. Graetzel, *Chem. Mater.* **2005**, *17*, 1248–1255.
- [36] V. D. Nithya, K. Pandi, Y. S. Lee, R. K. Selvan, *Electrochim. Acta* **2015**, *167*, 97–104.
- [37] Z. Ling, C. E. Ren, M.-Q. Zhao, J. Yang, J. M. Giamarco, J. Qiu, M. W. Barsoum, Y. Gogotsi, *P. Natl. Acad. Sci.* **2014**, *111*, 16676.
- [38] M.-Q. Zhao, C. E. Ren, Z. Ling, M. R. Lukatskaya, C. Zhang, K. L. Van Aken, M. W. Barsoum, Y. Gogotsi, *Adv. Mater.* **2015**, *27*, 339–345.
- [39] J. Luo, J. Zheng, J. Nai, C. Jin, H. Yuan, O. Sheng, Y. Liu, R. Fang, W. Zhang, H. Huang, Y. Gan, Y. Xia, C. Liang, J. Zhang, W. Li, X. Tao, *Adv. Funct. Mater.* **2019**, *29*, 1808107.
- [40] J. B. Cook, H.-S. Kim, Y. Yan, J. S. Ko, S. Robbenolt, B. Dunn, S. H. Tolbert, *Adv. Energy Mater.* **2016**, *6*, 1501937.
- [41] Z. Hu, L. Wang, K. Zhang, J. Wang, F. Cheng, Z. Tao, J. Chen, *Angew. Chem. Int. Ed.* **2014**, *53*, 12794–12798.
- [42] X. Xu, R. Zhao, W. Ai, B. Chen, H. Du, L. Wu, H. Zhang, W. Huang, T. Yu, *Adv. Mater.* **2018**, *30*, 1800658.
- [43] J. Dong, Y. Jiang, Q. Li, Q. Wei, W. Yang, S. Tan, X. Xu, Q. An, L. Mai, *J. Mater. Chem. A* **2017**, *5*, 10827–10835.
- [44] Y. Jiang, Y. Shen, J. Dong, S. Tan, Q. Wei, F. Xiong, Q. Li, X. Liao, Z. Liu, Q. An, L. Mai, *Adv. Energy Mater.* **2019**, *9*, 1900967.
- [45] H. Li, J. Lang, S. Lei, J. Chen, K. Wang, L. Liu, T. Zhang, W. Liu, X. Yan, *Adv. Funct. Mater.* **2018**, *28*, 1800757.
- [46] Q. Wei, Q. Li, Y. Jiang, Y. Zhao, S. Tan, J. Dong, L. Mai, D.-L. Peng, *Nano-Micro Lett.* **2021**, *13*, 55.
- [47] X. Deng, K. Zou, P. Cai, B. Wang, H. Hou, G. Zou, X. Ji, *Small Methods* **2020**, *4*, 2000401.
- [48] M. R. Lukatskaya, B. Dunn, Y. Gogotsi, *Nat. Commun.* **2016**, *7*, 12647.
- [49] Y.-G. Guo, J.-S. Hu, L.-J. Wan, *Adv. Mater.* **2008**, *20*, 2878–2887.
- [50] R. Malini, U. Uma, T. Sheela, M. Ganesan, N. G. Ranganathan, *Ionics* **2009**, *15*, 301–307.
- [51] J. Cabana, L. Monconduit, D. Larcher, M. R. Palacín, *Adv. Mater.* **2010**, *22*, E170–E192.
- [52] W. Qi, J. G. Chapter, Q. Wu, T. Yin, G. Gao, D. Cui, *J. Mater. Chem. A* **2017**, *5*, 19521–19540.
- [53] Y. Li, Y. Lu, P. Adelhelm, M.-M. Titirici, Y.-S. Hu, *Chem. Soc. Rev.* **2019**, *48*, 4655–4687.
- [54] Y. Moritomo, M. Takachi, Y. Kurihara, T. Matsuda, *Adv. Mater. Sci. Eng.* **2013**, *2013*, 967285.
- [55] Y. C. Song, A. K. Soh, J. Q. Zhang, *J. Mater. Sci.* **2016**, *51*, 9902–9911.
- [56] J. Chen, Q. Li, T. P. Pollard, X. Fan, O. Borodin, C. Wang, *Mater. Today* **2020**, *39*, 118–126.
- [57] Y. Zhu, C. Wang, *J. Power Sources* **2011**, *196*, 1442–1448.
- [58] F. Klein, B. Jache, A. Bhide, P. Adelhelm, *Phys. Chem. Chem. Phys.* **2013**, *15*, 15876–15887.
- [59] C. Wang, L. Wang, F. Li, F. Cheng, J. Chen, *Adv. Mater.* **2017**, *29*, 1702212.
- [60] O. Munteşari, J. Lau, A. Likitchatchawankun, B.-A. Mei, C. S. Choi, D. Butts, B. S. Dunn, L. Pilon, *Electrochim. Acta* **2019**, *307*, 512–524.
- [61] G. Leftheriotis, S. Papaefthimiou, P. Yianoulis, *Solid State Ionics* **2007**, *178*, 259–263.
- [62] M. J. Lee, K. Lee, J. Lim, M. Li, S. Noda, S. J. Kwon, B. DeMattia, B. Lee, S. W. Lee, *Adv. Funct. Mater.* **2021**, *n/a*, 2009397.
- [63] M. Z. Iqbal, S. S. Haider, S. Siddique, M. R. A. Karim, S. Zakar, M. Tayyab, M. M. Faïsal, M. Sulman, A. Khan, M. Baghayeri, M. A. Kamran, T. Alherbi, M. J. Iqbal, T. Hussain, *J. Energy Storage* **2020**, *27*, 101056.
- [64] A. Rudola, K. Saravanan, C. W. Mason, P. Balaya, *J. Mater. Chem. A* **2013**, *1*, 2653–2662.
- [65] H.-K. Roh, M.-S. Kim, K. Y. Chung, M. Ulaganathan, V. Aravindan, S. Madhavi, K. C. Roh, K.-B. Kim, *J. Mater. Chem. A* **2017**, *5*, 17506–17516.

- [66] K. Lan, Q. Wei, R. Wang, Y. Xia, S. Tan, Y. Wang, A. Elzatahry, P. Feng, L. Mai, D. Zhao, *J. Am. Chem. Soc.* **2019**, *141*, 16755–16762.
- [67] P. Oh, H. Lee, S. Park, H. Cha, J. Kim, J. Cho, *Adv. Energy Mater.* **2020**, *10*, 2000904.
- [68] J. Lu, Y. Lei, K. C. Lau, X. Luo, P. Du, J. Wen, R. S. Assary, U. Das, D. J. Miller, J. W. Elam, H. M. Albishri, D. A. El-Hady, Y.-K. Sun, L. A. Curtiss, K. Amine, *Nat. Commun.* **2013**, *4*, 2383.
- [69] J. Luo, C. Fang, C. Jin, H. Yuan, O. Sheng, R. Fang, W. Zhang, H. Huang, Y. Gan, Y. Xia, C. Liang, J. Zhang, W. Li, X. Tao, *J. Mater. Chem. A* **2018**, *6*, 7794–7806.
- [70] Q. Wu, J. Xu, X. Yang, F. Lu, S. He, J. Yang, H. J. Fan, M. Wu, *Adv. Energy Mater.* **2015**, *5*, 1401756.
- [71] H. Ren, R. Yu, J. Qi, L. Zhang, Q. Jin, D. Wang, *Adv. Mater.* **2019**, *31*, 1805754.
- [72] L. Wu, D. Bresser, D. Buchholz, G. A. Giffin, C. R. Castro, A. Ochel, S. Passerini, *Adv. Energy Mater.* **2015**, *5*, 1401142.
- [73] Z.-L. Xu, K. Lim, K.-Y. Park, G. Yoon, W. M. Seong, K. Kang, *Adv. Funct. Mater.* **2018**, *28*, 1802099.
- [74] F. A. Soto, P. Yan, M. H. Engelhard, A. Marzouk, C. Wang, G. Xu, Z. Chen, K. Amine, J. Liu, V. L. Sprengle, F. El-Mellouhi, P. B. Balbuena, X. Li, *Adv. Mater.* **2017**, *29*, 1606860.
- [75] K. Li, J. Zhang, D. Lin, D.-W. Wang, B. Li, W. Lv, S. Sun, Y.-B. He, F. Kang, Q.-H. Yang, L. Zhou, T.-Y. Zhang, *Nat. Commun.* **2019**, *10*, 725.
- [76] Y. Mei, Y. Huang, X. Hu, *J. Mater. Chem. A* **2016**, *4*, 12001–12013.
- [77] J. Ni, S. Fu, Y. Yuan, L. Ma, Y. Jiang, L. Li, J. Lu, *Adv. Mater.* **2018**, *30*, 1704337.
- [78] X. Xu, B. Chen, J. Hu, B. Sun, X. Liang, N. Li, S. A. Yang, H. Zhang, W. Huang, T. Yu, *Adv. Mater.* **2019**, *31*, 1904589.
- [79] S. Zhang, H. Tan, X. Rui, Y. Yu, *Acc. Chem. Res.* **2020**, *53*, 1660–1671.
- [80] X. Xu, F. Xiong, J. Meng, X. Wang, C. Niu, Q. An, L. Mai, *Adv. Funct. Mater.* **2020**, *30*, 1904398.
- [81] H. Huang, D. Kundu, R. Yan, E. Tervoort, X. Chen, L. Pan, M. Oschatz, M. Antonietti, M. Niederberger, *Adv. Energy Mater.* **2018**, *8*, 1802800.
- [82] H. Huang, T. Tian, L. Pan, X. Chen, E. Tervoort, C.-J. Shih, M. Niederberger, *J. Mater. Chem. A* **2019**, *7*, 16109–16116.
- [83] J. Dong, Y. He, Y. Jiang, S. Tan, Q. Wei, F. Xiong, Z. Chu, Q. An, L. Mai, *Nano Energy* **2020**, *73*, 104838.
- [84] W. Sun, X. Tang, Y. Wang, *Electrochem. Energy Rev.* **2020**, *3*, 127–154.
- [85] G. Barik, S. Pal, *Phys. Chem. Chem. Phys.* **2020**, *22*, 1701–1714.
- [86] Y.-C. Lin, D. O. Dumcenco, Y.-S. Huang, K. Suenaga, *Nat. Nanotechnol.* **2014**, *9*, 391–396.
- [87] X. Wang, X. Shen, Z. Wang, R. Yu, L. Chen, *ACS Nano* **2014**, *8*, 11394–11400.
- [88] J. Park, J.-S. Kim, J.-W. Park, T.-H. Nam, K.-W. Kim, J.-H. Ahn, G. Wang, H.-J. Ahn, *Electrochim. Acta* **2013**, *92*, 427–432.
- [89] L. Huang, Q. Wei, X. Xu, C. Shi, X. Liu, L. Zhou, L. Mai, *Phys. Chem. Chem. Phys.* **2017**, *19*, 13696–13702.
- [90] K. Zhang, P. Li, S. Guo, J. Y. Jeong, B. Jin, X. Li, S. Zhang, H. Zeng, J. H. Park, *J. Mater. Chem. A* **2018**, *6*, 22513–22518.
- [91] P. Li, J. Y. Jeong, B. Jin, K. Zhang, J. H. Park, *Adv. Energy Mater.* **2018**, *8*, 1703300.
- [92] M. Naguib, M. Kurtoglu, V. Presser, J. Lu, J. Niu, M. Heon, L. Hultman, Y. Gogotsi, M. W. Barsoum, *Adv. Mater.* **2011**, *23*, 4248–4253.
- [93] M. Naguib, O. Mashtalir, J. Carle, V. Presser, J. Lu, L. Hultman, Y. Gogotsi, M. W. Barsoum, *ACS Nano* **2012**, *6*, 1322–1331.
- [94] M. Naguib, J. Halim, J. Lu, K. M. Cook, L. Hultman, Y. Gogotsi, M. W. Barsoum, *J. Am. Chem. Soc.* **2013**, *135*, 15966–15969.
- [95] M. Naguib, V. N. Mochalin, M. W. Barsoum, Y. Gogotsi, *Adv. Mater.* **2014**, *26*, 992–1005.
- [96] J. Nan, X. Guo, J. Xiao, X. Li, W. Chen, W. Wu, H. Liu, Y. Wang, M. Wu, G. Wang, *Small* **2019**, *n/a*, 1902085.
- [97] Y.-J. Lei, Z.-C. Yan, W.-H. Lai, S.-L. Chou, Y.-X. Wang, H.-K. Liu, S.-X. Dou, *Electrochem. Energy Rev.* **2020**, *3*, 766–792.
- [98] S. Kajiyama, L. Szabova, K. Sodeyama, H. Iinuma, R. Morita, K. Gotoh, Y. Tateyama, M. Okubo, A. Yamada, *ACS Nano* **2016**, *10*, 3334–3341.
- [99] M. R. Lukatskaya, O. Mashtalir, C. E. Ren, Y. Dall'Agnese, P. Rozier, P. L. Taberna, M. Naguib, P. Simon, M. W. Barsoum, Y. Gogotsi, *Science* **2013**, *341*, 1502.
- [100] X. Xie, M.-Q. Zhao, B. Anasori, K. Maleski, C. E. Ren, J. Li, B. W. Byles, E. Pomerantseva, G. Wang, Y. Gogotsi, *Nano Energy* **2016**, *26*, 513–523.
- [101] Q. Sun, Z.-W. Fu, *Electrochim. Acta* **2008**, *54*, 403–409.
- [102] J. Yuan, X. Hu, J. Chen, Y. Liu, T. Huang, Z. Wen, *J. Mater. Chem. A* **2019**, *7*, 9289–9296.
- [103] J. Li, H. Wang, X. Xiao, *Energy Environ. Mater.* **2020**, *3*, 306–322.
- [104] H. Wang, J. Li, K. Li, Y. Lin, J. Chen, L. Gao, V. Nicolosi, X. Xiao, J.-M. Lee, *Chem. Soc. Rev.* **2021**, *50*, 1354–1390.
- [105] X. Li, A. L. Hector, J. R. Owen, S. I. U. Shah, *J. Mater. Chem. A* **2016**, *4*, 5081–5087.
- [106] L. Wang, J. Sun, R. Song, S. Yang, H. Song, *Adv. Energy Mater.* **2016**, *6*, 1502067.
- [107] Y. Jiang, J. Dong, S. Tan, Q. Wei, F. Xiong, W. Yang, Y. Shen, Q. Zhang, Z. Liu, Q. An, L. Mai, *J. Energy Chem.* **2021**, *55*, 295–303.
- [108] Z. Xing, Q. Liu, A. M. Asiri, X. Sun, *Adv. Mater.* **2014**, *26*, 5702–5707.
- [109] S. T. Oyama, T. Gott, H. Zhao, Y.-K. Lee, *Catal. Today* **2009**, *143*, 94–107.
- [110] L.-F. Que, F.-D. Yu, K.-W. He, Z.-B. Wang, D.-M. Gu, *Chem. Mater.* **2017**, *29*, 9133–9141.
- [111] X. Liu, G. A. Elia, B. Qin, H. Zhang, P. Ruschhaupt, S. Fang, A. Varzi, S. Passerini, *ACS Energy Lett.* **2019**, *4*, 2675–2682.
- [112] N. Kurra, M. Alhabeb, K. Maleski, C.-H. Wang, H. N. Alshareef, Y. Gogotsi, *ACS Energy Lett.* **2018**, *3*, 2094–2100.
- [113] H. Sun, L. Mei, J. Liang, Z. Zhao, C. Lee, H. Fei, M. Ding, J. Lau, M. Li, C. Wang, X. Xu, G. Hao, B. Papandrea, I. Shakir, B. Dunn, Y. Huang, X. Duan, *Science* **2017**, *356*, 599.
- [114] K. Zou, P. Cai, Y. Tian, J. Li, C. Liu, G. Zou, H. Hou, X. Ji, *Small Methods* **2020**, *4*, 1900763.
- [115] R. Wang, S. Wang, X. Peng, Y. Zhang, D. Jin, P. K. Chu, L. Zhang, *ACS Appl. Mater. Interfaces* **2017**, *9*, 32745–32755.
- [116] Z. Le, F. Liu, P. Nie, X. Li, X. Liu, Z. Bian, G. Chen, H. B. Wu, Y. Lu, *ACS Nano* **2017**, *11*, 2952–2960.
- [117] Y.-E. Zhu, L. Yang, J. Sheng, Y. Chen, H. Gu, J. Wei, Z. Zhou, *Adv. Energy Mater.* **2017**, *7*, 1701222.
- [118] X. Wang, S. Kajiyama, H. Iinuma, E. Hosono, S. Oro, I. Moriguchi, M. Okubo, A. Yamada, *Nat. Commun.* **2015**, *6*, 6544.

Manuscript received: February 9, 2021

Revised manuscript received: March 23, 2021

Accepted manuscript online: March 28, 2021

Version of record online: April 9, 2021